Materials & Design 265 (2026) 115952

Contents lists available at ScienceDirect

Materials & Design

journal homepage: www.elsevier.com/locate/matdes

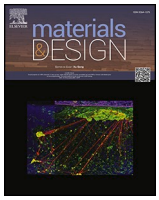

Tailored highly transparent porous silica coatings for enhanced optical and mechanical performance of solar covers

Naia Barandica [a,b], Gema San Vicente [a,*], Ignacio Torres [c], Alenka Ristić [d], Aránzazu Fernández-García [e]

[a] CIEMAT-PSA. Materials for Concentrating Solar Thermal Technologies Unit. Avenida Complutense 40, Madrid 28040, Spain
[b] Universidad Autónoma de Madrid. Escuela de Doctorado. Ciudad Universitaria de Cantoblanco, Madrid 28049, Spain
[c] CIEMAT. Energy and Environmental Devices Unit. Avenida Complutense 40, Madrid 28040 Spain
[d] National Institute of Chemistry Slovenia, Department of Inorganic Chemistry and Technology, Hajdrihova 19, 1000 Ljubljana, Slovenia
[e] CIEMAT-Plataforma Solar de Almería, Ctra. de Senés km. 4,5, Almería, Spain

ARTICLE INFO

Keywords:
Solar application
Glass cover
Anti-reflective coating
Porous material
Dip-coating
Pore-generator

ABSTRACT

Sol-gel porous silica-based anti-reflective coatings (AR) represent a key solution to minimize reflectance losses and improve solar systems efficiency. However extreme climatic conditions compromise the long-term durability of the coatings. This study focuses on the impact of pore-forming agent (Pluronic® P-123) concentration, thermal treatment, and silicon precursor ratio on optical, structural, and environmental durability properties. The introduction of Pluronic® reduced the refractive index, achieving a minimum value of 1.215 at 600 nm, corresponding to a porosity of 56 %, and increased optical transparency, with transmittance reaching 99.8 % at 600 nm. However, higher porosity minimized mechanical stability, with abrasion resistance decreasing as Pluronic® concentration increased. Prolonged (1 h) thermal treatments at 500 °C led to excessive burnout of the Pluronic®, reducing mechanical resistance. Modifying the silicon precursor ratio (TEOS:MTES) impacts coating density, while both silicon precursor ratio and Pluronic® concentration influence the coatings' environmental durability. These findings highlight the importance of achieving a balance between optical performance and mechanical/environmental durability. Optimal balanced performance was achieved with 2 % v/v Pluronic® and TEOS:MTES ratio of 70:30. By carefully controlling the formulation and processing parameters, AR coatings properties can be tailored for solar applications, ensuring high efficiency and stability under operational conditions.

1. Introduction

As global energy demand rises and the shift toward renewable sources accelerates, it is essential to optimize and reduce the cost of these technologies to ensure their viability and attractiveness. One effective strategy is extending the accuracy of critical components to match the expected lifetime of the installations, thereby improving cost efficiency [1]. Among renewables, solar energy is one of the fastest growing and most cost-effective options. This growth is closely linked to the development of advanced materials that enhance the performance of clean energy devices.

In the utilization of solar energy, the main technologies can be broadly classified into three categories: (1) photovoltaic (PV) system which is the most widely deployed [2], (2) non-concentrated solar thermal system and (3) concentrated solar thermal (CST) technology. Beyond conventional uses, solar energy also enables direct applications like solar desalination, offering sustainable and low–cost solutions for harnessing renewable power [3].

PV systems have become widely adopted due to their versatility and their ability to convert solar radiation directly into electricity [4]. Talking about materials, beyond traditional silicon, recent literature has extensively explored novel compounds such as perovskites [5] or metallic oxides that combined with silicon give place to novel hybrid photovoltaic systems [6]. These materials are revolutionizing opto-electronic and photovoltaic systems due to their tunable bandgaps, while also showing great promise in thermoelectric applications for heat-to-electricity conversion [5].

Non-concentrating solar thermal systems efficiently produce heat at temperatures up to approximately 125 °C, whereas CST technologies operate at higher temperatures up to 550 °C. This temperature range enables their application both in industrial process heat and in

* Corresponding author.
E-mail address: gema.sanvicente@ciemat.es (G.S. Vicente).

https://doi.org/10.1016/j.matdes.2026.115952
Received 14 January 2026; Received in revised form 12 March 2026; Accepted 31 March 2026
Available online 7 April 2026

Nomenclature

Abbreviations

AR	Anti-reflective
BEMA	Bruggeman Effective Medium Approximation
BET	Brunauer-Emmett-Teller
CST	Concentrating solar thermal
CTAB	Cetyltrimethylammonium bromide
DFT	Density functional theory
DTA	Differential thermal analysis
ETOH	Ethanol
FE-SEM	Field emission scanning electron microscope
ISO	International Organization for Standardization
MTES	Methyltriethoxysilane
NIR	Near Infrared (0.8–2.5 μm)
PSDs	Pore size distributions
PV	Photovoltaic
PVD	Physical vapor deposition
TEOS	Tetraethyl orthosilicate
TGA	Thermogravimetric analysis
UV	Ultraviolet (100–380 nm)
VIS	Visible (380–760 nm)
WCA	Water contact angle (°)

Symbols

r_w	Withdrawal rate (cm/min)
T	Temperature (℃)
λ	Wavelength (μm, nm)
P	Porosity (%)
d	Thickness (nm)
μ	Viscosity (cP)
R	Reflectance (%)
n	Refractive index (−)
θ_i	Incidence angle ()
λ_0	Wavelength of the incident light (μm, nm)
V_t	Total pore volume (cm^3/g)
τ_s	Solar transmittance (%, 1)
S_{BET}	Specific surface area (m^2/g)
w_{max}	Pore diameter as the maximum of the pore size distribution (nm)
τ_h	Hemispherical transmittance (%)
ρ_h	Hemispherical reflectance (%)
$\tau_{\lambda,h}$	Spectral hemispherical transmittance (−)
G_b	Solar spectral irradiance ($W/m^2{\cdot}nm$)
R_a	Average surface roughness (μm)
p/p_0	Relative pressure (−)

electricity generation through power cycles similar to those used in conventional power plants.

Among CST configurations, parabolic-trough collectors represent the most mature and widely deployed technology in commercial CST installations. As solar energy is concentrated 70–100 times in the system, the working temperature ranges between 125 and 550 °C [7]. To minimize thermal losses and protect the absorber, the receiver is enclosed within a glass cover. Optical properties directly influence the amount of solar radiation transmitted to the absorber and, consequently, the overall efficiency of the system.

Similarly, both PV and non-concentrating solar thermal systems incorporate a glass cover: in PV systems it protects the solar cells, while in non-concentrating thermal systems it protects the absorber plate.

Optical reflection is a fundamental phenomenon that occurs when light propagates through an interface between two media with different refractive indices. Solar systems with a front glass (photovoltaic non-concentrating solar thermal and concentrated solar thermal systems) lose around 8–10 % of the incident solar energy because of reflection, depending on the type of glass [8]. Anti-reflective (AR) coatings have been effectively used in renewable technologies to reduce these losses, thereby improving energy conversion [9,10]. While surface texturing is an alternative, porous single-layer coating remains the most viable solution for large-scale solar glass due to their optical versatility. According to the Fresnel equations [11–13], when light transitions between media of different refractive index (n), part of the light is reflected, while the rest is transmitted. The amount of reflected light depends on the refractive index of the two media and the angle of incidence. At normal incidence, the reflectance (R) at an interface can be simplified using the reduced Fresnel equation (Eq. 1):

$$R = \left(\frac{n_1 - n_2}{n_1 + n_2}\right)^2$$

where n_1 and n_2 are the refractive index of the two media. For example, when light travels from air ($n \approx 1$) to glass ($n \approx 1.5$), the reflectance at normal incidence is approximately 4 % (in each side of the glass). To minimize reflections, an AR layer can be deposited on the glass-cover surface, with a refractive index value given by the geometric mean of the refractive indices of the surrounding media (Eq. (2) and a thickness (d) that satisfies the quarter wavelength condition (Eq. (3):

$$nAR = \sqrt{n_{glass} \cdot n_{air}} \tag{2}$$

$$d = \frac{\lambda_0}{4 n_{AR}} \tag{3}$$

where λ_0 is the selected wavelength of the incident light, and n_{AR} is the refractive index of the AR layer.

This thickness ensures that the reflected light waves from the top and bottom surfaces of the AR layer are out of phase by 180° ($\lambda/2$), resulting in destructive interference and thus reducing the overall reflectance. The choice of refractive index helps balance the impedance mismatch between the two media, further enhancing the interference effect and improving light transmission through the coated surface.

Fig. 1illustrates the operational principle of an AR coating applied to both sides of a borosilicate-glass substrate. This design involves negligible optical losses, at the selected λ, with de correct n and d, which define the amplitude and phase of the reflected beams in both sides of the coatings.

SiO_2 is the material commonly used as AR coating for glass with, $n \approx 1.45$ [14,15]. The introduction of porosity (P) in the coating is an effective way to reduce the effective n and reach the required condition ($n = 1.22$), enhancing the optical performance of the solar system [16].

The preparation of AR coatings can be carried out using various techniques, including vacuum methods such as physical vapor deposition (PVD) [17] and simpler, sol–gel methods with dip-coating [18–20] and spin-coating [21]. In this study, the dip-coating method is employed due to its simplicity, consideration as green alternative [22], low cost, and the ability to uniformly coat both sides of the substrate at the same time [23]. Dip-coating involves immersing the substrate vertically in the sol–gel solution and withdrawing it at a controlled speed (r_w), forming a uniform film as the solvent evaporates. Based on the Landau-Levich principle, the film thickness in this method depends on both the r_w and the viscosity (μ) of the solution [24]. Higher r_w produces thicker films. On the other hand, the use of a solution with higher viscosity gives place to thicker films deposited at the same r_w than others prepared from solutions with lower viscosity. Since the composition of the solutions affects its viscosity, the, r_w must be specifically adjusted for each formulation. This precise adjustment of the speed for each case ensures that all coatings reach the target d required for optimal optical

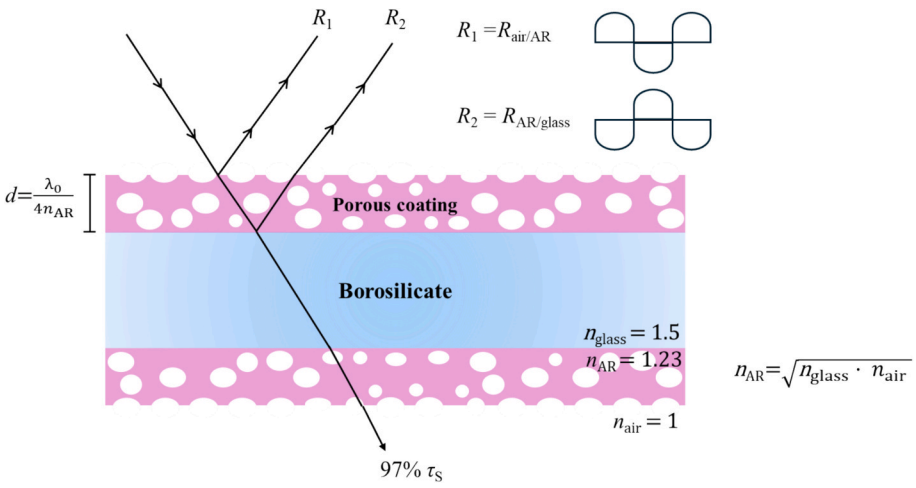

Fig. 1. Schematic of the operational principle of an anti-reflective coating applied to both sides of a borosilicate glass surface, showing the destructive interference conditions.

performance. The formation of porous structure in the SiO_2 coating by using porosity generators in the sol–gel process [25], is illustrated in Fig. 2. The sol–gel method starts with a solution containing a silica precursor, water, a solvent such as ethanol (EtOH) and a catalyst to facilitate the hydrolysis and condensation reactions. During these reactions, a silica network forms, incorporating the solvent and water, which is later removed during a heat treatment. To reduce the *n* of the silica films to the desire value, pores can be introduced/created within the structure during film preparation. Porosity is typically achieved through the addition of pore-forming agents, including surfactants such as Triton® X-100 [26], Pluronic® P-123 [16], CTAB (cetyltrimethylammonium bromide) [27], and Pluronic® F-127 [28]. These surfactants act as templates, controlling pore formation within the silica matrix and allowing for a tunable pore size distribution. The selection of the specific porogen is critical, as it dictates the final pore architecture and mechanical stability [29]. While CTAB often leads to fine mesoporous structures, it can result in coatings with limited mechanical robustness. In contrast, Pluronic® P-123, a triblock copolymer, offers a unique rationale for selection due to its higher molecular weight and ability to form larger, more stable micellar templates compared to F-127 or ionic surfactants [30]. This choice results in a superior balance between the reduction of the refractive index and the preservation of the structural integrity of the silica framework, which is essential for outdoor durability. In the calcination step, any organic residual is removed, resulting in a stable, amorphous porous silica.

Although introducing porosity enhances the AR layer's optical properties, it also introduces several challenges. The porous structure is capable of increasing the coating's sensitivity to moisture, leading to water absorption, which may compromise long-term performance [31,32]. Additionally, the porous nature makes the surface more susceptible to dirt accumulation, potentially affecting optical quality and requiring regular cleaning [33]. Finally, coating mechanical resistance and adhesion to the substrate can be committed. Thus, modulating parameters, such as surfactant selection and the silica precursors ratio, is crucial for tailoring the optical properties, mechanical hardness, wettability, and pore size distribution of AR coatings. These characteristics are essential for enhancing durability and optimizing the functional performance of AR coatings under real operation conditions [34,35].

Different surfactants are able to promote either open or closed porosity. Open porosity typically increases the surface area and promote hydrophilicity, leading to higher wettability and making the coating

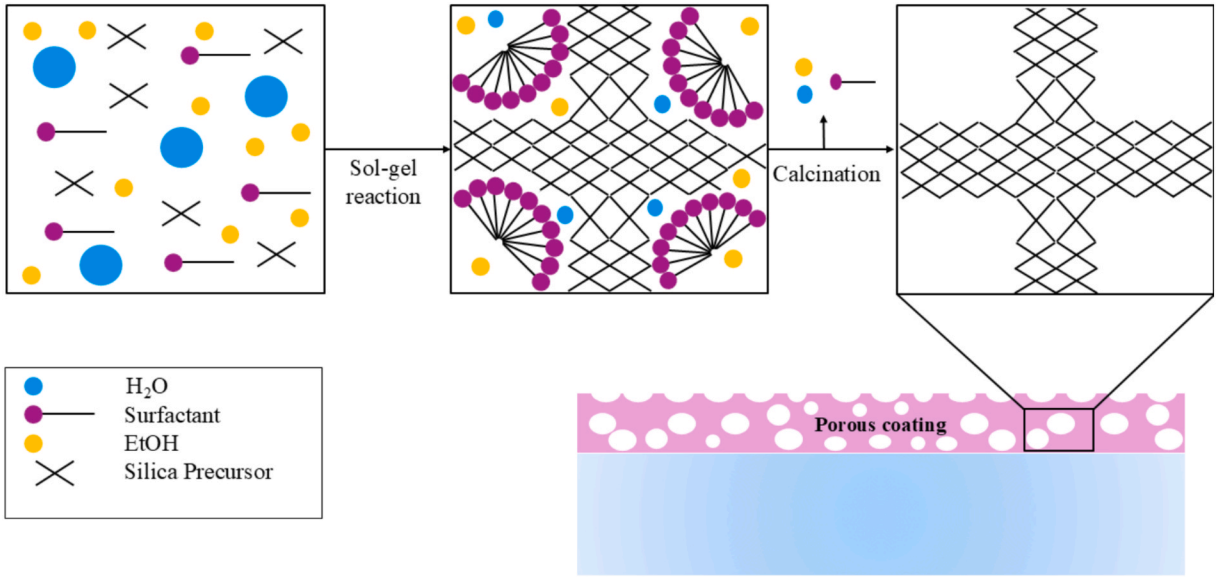

Fig. 2. Schematic representation of the sol–gel process used to create a porous structure in anti-reflective coatings.

more self-cleaning by allowing water to spread across the surface and wash away contaminants. However, the fill of pores with water may also increase the refractive index, changing the AR behavior. Closed porosity, in contrast, is able provide greater durability and hardness, making the coating more resistant to mechanical wear, but potentially more susceptible to dirt accumulation [32,36].

The selection and ratio of silica precursors such as methyltriethoxysilane (MTES) or tetraethyl orthosilicate (TEOS) is another critical factor that influences the structural properties of the coating. Higher MTES content is able to increase the organic component of the silica network, resulting in a more flexible and hydrophobic layer, which may reduce wettability but improve the coating's resistance to moisture absorption. Adjusting the TEOS:MTES ratio also affects pore size. A higher MTES ratio typically leads to larger pore sizes, which can reduce overall hardness due to increased porosity but may enhance light scattering and decrease refractive index [37,38].

This work investigates the development of durable and optically efficient AR coatings for glass covers of solar technologies by using Pluronic® P-123 as pore generator. Previous works were made by this research team using Triton® as pore generator yielding and an appropriate optical property. However, the resulting surfaces were highly reactive and prone to adsorb species within the porous network [26,39]. The utilization of P-123 in this study is specifically aimed at overcoming these limitations by generating a more controlled mesoporous network that minimizes reactive sites while maintaining the low refractive index required for high-performance solar applications. The current study deeply examines the influence of pore-former concentration, thermal treatment conditions, and TEOS:MTES precursor ratios, aiming to strike a balance between mechanical durability and optical efficiency. A detailed characterization of the coatings was performed, including optical and structural analysis, as well as accelerated aging tests, such as abrasion resistance, condensation exposure, and UV degradation. While most previous research has primarily focused on achieving coating with adequate optical properties, this work expands the understanding of AR coatings by evaluating their resistance to environmental stressors, contributing to their optimization for long-term performance in solar applications.

2. Materials and experimental methodology

In this section, the formation of the gels and the subsequent characterization techniques of the resulting coatings are presented.

2.1. Materials

TEOS, 98 % and MTES, ≥ 99 % from Sigma Aldrich were employed as silica precursors. Absolute ethanol was used as solvent and deionized water was applied as hydrolysis agent for silica precursors. Sulfuric acid (H_2SO_4, 97 %) was obtained from Panreac and utilized as catalyzing agent. Pluronic® P-123 (PEG-PPG-PEG, $M_n \sim 5{,}800$) was acquired from Sigma Aldrich as a pore generator agent. The coatings were deposited on 3-mm-thickness borosilicate glass substrates and polished silicon wafers.

2.2. Preparation of AR films

The sol–gel solution was prepared by mixing TEOS, MTES, ethanol and deionized water in the presence of sulfuric acid as a catalyst. The molar ratio of alkoxides:ethanol:water was 1:20:4.1. The mixture was stirred for 24 h to promote hydrolysis and condensation reactions. Next, Pluronic® was added together with ethanol to dilute the solution. As increasing Pluronic® content raised the μ of the solution, the withdrawal rate was adjusted (KSV NIMA dip coater) for each solution in order to achieve the optimal thickness to obtain the desired effective refractive index. All samples underwent thermal treatment at 500 °C for 15 min or 1 h to evaluate the effect of the thermal treatment on the final coating properties.

2.3. Optical and structural characterization

The effect of the molar ratios of the silica precursors (TEOS:MTES) was studied by adjusting them to 50:50, 70:30, and 90:10, with Pluronic® concentration maintained at 2.5 % v/v. The samples prepared with these solutions were labelled as P-5:5, P-7:3, and P-9:1, respectively. Additionally, Pluronic® concentrations were varied between 0 and 3.3 % v/v, with the TEOS:MTES ratio fixed at 50:50, resulting in solutions named P-0, P-0.5, P-1, P-1.5, P-2, P-2.5, P-2.8 and P-3.3, where the numbers after the hyphen detail the Pluronic® concentration. Stability of the solutions was studied by viscosity measurements carried out at 22 °C using a SELECTA rotational viscometer equipped with a low viscosity adapter and a water jacket for precise temperature control. They were stored at ambient temperature in closed containers, and their viscosity was monitored over a total period of 252 days.

Hemispherical transmittance (τ_h) spectra of the samples were measured at room temperature using a Perkin-Elmer LAMBDA 950 UV–VIS-NIR double-beam spectrophotometer equipped with a 150-mm diameter integrating sphere. The solar transmittance (τ_s) was calculated by integrating the measured transmittance spectra over the standard direct AM1.5 solar spectral irradiance (ASTM G173-03), according to IEC-TS-62862–1-1 standard [40]. The τ_s is computed using the following equation (Eq. (4):

$$\tau s = \frac{\int_{\lambda_1}^{\lambda_2} \tau_{\lambda,h} G_b d\lambda}{\int_{\lambda_1}^{\lambda_2} G_b(\lambda) d\lambda} \tag{4}$$

where $\tau_{\lambda,h}(\lambda)$ is the measured spectral hemispherical transmittance at a given wavelength λ, and $G_b(\lambda)$ represents the solar spectral irradiance at that λ. The λ range used for these measurements was 300 nm to 2500 nm, covering ultraviolet, visible, and near-infrared regions.

The refractive index of the coatings was measured using a SEMILAB SE2000 ellipsometer, operating at an incidence angle of 75°. The AR coatings to be characterized with this equipment were deposited on polished monocrystalline silicon wafers, providing a smooth and uniform substrate, ideal for precise optical measurements. In addition, the hemispherical reflectance (ρ_h) of the silicon wafers was measured over the spectral range of 300–2500 nm.

To extract n, the Cauchy dispersion model was applied, which is particularly suitable for transparent materials like AR coatings [41]. The Cauchy model describes the refractive index as a function of λ (Eq. (5):

$$n(\lambda) = A + \frac{B}{\lambda^2} + \frac{C}{\lambda^4} \tag{5}$$

where A, B, and C are constants specific to the material, and λ is the wavelength of light. By fitting the experimental data to this model, accurate values for the films thickness and the refractive index across the λ range were obtained. This approach is well-established in thin film analysis due to its simplicity and effectiveness for transparent or weakly absorbing films [42].

The surface wettability of the samples was studied by static water contact angle (WCA) measurements using a KSV CAM 200 instrument and distilled water. Three measurements were made for each of the three replicates of each chemical solution used for coating. Thus, for each chemical solution, nine measurements were taken in order to provide representative standard deviation values.

To estimate the porosity (P) of the AR coatings, a theoretical approach was employed based on the relationship between the refractive index and porosity. The most common approximation used for such calculations is the Bruggeman Effective Medium Approximation (BEMA) [43]. BEMA models the effective refractive index of a composite material by combining the contributions of its components, proportioning them according to their volume fractions, while also considering their dielectric interactions. In this context, models that represent pores as embedded particles of air within the material can be used to calculate

the effective refractive index [8]. P may be expressed as:

$$P = 1 - \frac{{n_{porous}}^2 - 1}{{n_{non-porous}}^2 - 1} \cdot 100 \quad (6)$$

where P is the porosity %, n_{porous} is the refractive index of the porous coating, obtained experimentally and $n_{\text{non-porous}}$ is the refractive index of the bulk, non-porous silica material. This simplified model, while not accounting for all potential interactions or structural complexities, provides a practical estimation of the porosity based on measured refractive indices.

2.4. Thermal analysis study

The thermal analysis of powders obtained from the precursor solutions was done using thermogravimetric analysis (TGA) and differential thermal analysis (DTA). The measurements were carried out from room temperature up to 700 °C, with a heating rate of 10 °C/min in air atmosphere with a flow rate of 100 ml/min. Platinum crucibles were used for sample containment, and the experiments were performed using a SDT Q600 from TA Instruments.

2.5. Porosity and surface morphology characterization

The structural properties of powdered samples were evaluated through nitrogen adsorption isotherms, measured using an Autosorb iQ3 (Quantachrome Instruments, Boynton Beach, FL, USA). For obtaining the powdered samples, each precursor solution was subjected to a thermal treatment at 500 °C for 15 min, following the same protocol used for the samples deposited as films. The adsorption isotherms were recorded at a constant temperature of −196 °C, with prior outgassing of the samples under vacuum conditions at 150 °C for several hours to remove any adsorbed impurities that might affect nitrogen adsorption [44,45].

Specific surface area (S_{BET}), was calculated using the Brunauer-Emmett-Teller (BET) method based on the adsorption data in the relative pressure (p/p_0) range from 0.1 to 0.25 [46]. The total pore volume (V_t), was determined from the amount of nitrogen adsorbed at a relative pressure of 0.95 [47]. The pore size distributions (PSDs) were calculated from N_2 adsorption data by the built-in algorithm based on density functional theory (DFT) method [48,49]. This method allowed for differentiation of pore size contributions. The maxima on the PSDs are considered as the micro or mesopore diameters for given samples.

A high-resolution field emission scanning electron microscope (FE-SEM), model FEI VERIOS 460, operating at an accelerating voltage of 2 kV, was utilized to examine the surface morphology of the coatings (Table 1).

Table 1
Silica precursor molar ratio and Pluronic® concentration of all the solutions studied.

Name	TEOS (molar ratio)	MTES (molar ratio)	Pluronic® (% v/v)
P-0	50	50	–
P-0.5	50	50	0.5
P-1	50	50	1
P-1.5	50	50	1.5
P-2	50	50	2
P-2.5	50	50	2.5
P-2.8	50	50	2.8
P-3.3	50	50	3.3
P-50:50	50	50	2.5
P-70:30	70	30	2.5
P-90:10	90	10	2.5

2.6. Environmental and weather resistance

The accelerated aging tests were carried out in a climate chamber under two different conditions. The tests were selected to replicate the plants' climatic conditions as accurately as possible and to reproduce them with maximum accuracy. The first condition involved exposure to condensation according to IEC TS 62862–3-3 standard [50]. The second condition combined UV radiation and condensation. The combined test consisted of 12-hour cycles, including 8 h exposure to UV radiation at 60 °C, followed by 15 min of water spray, and then condensation at 50 °C for 3 h and 45 min.

Abrasion tests were conducted using a Taber 5750 linear abrasion tester, following the test conditions specified in the IEC TS 62862–3–3–3 technical specification [50]. These conditions included a stroke length of 40 mm and a speed of 7 cycles/min, and an abrasive material conformed to the MIL-E12397 standard. However, a higher weight was applied to accelerate the abrasion process (750 g instead of 350 g). Three abrasion grooves were made on each sample for every block of cycles performed, in order to obtain enough surface to perform the optical characterization of the abraded surface.

The abrasion marks produced by the abrasion tests were characterized by profilometry, making use of a Dektak 150 profilometer. Three linear sweeps per sample of 0.6 mm in length were performed with a diamond tip of 2 μm diameter and a load of 1 mg. The average surface roughness (R_a) was calculated according to ISO 21920–2:2021[51].

In addition, all these samples were observed with a Leica DM4 M optical microscope, with image acquisition system and software for their analysis and characterization of the damage produced on their surfaces, as well as their optical characterization, after each block of abrasion cycles performed.

The scratch resistance of the coating was evaluated using a commercial pencil hardness tester (Scratch Hardness Tester PH1100, NEURTEK). The procedure was carried out in accordance with ASTM Standard D3360-00 [52]. The test is performed by applying a constant load of 750 g at a 45° angle relative to the horizontal film surface while the pencil is drawn across the coated sample [53]. The test classifies surface resistance to scratching on a standardized scale ranging from 9B (softest) to 9H (hardest).

3. Results and discussion

In this section, the results of the study are presented. First, the effects of varying the concentration of the pore-forming agent and the thermal treatment duration (15 min and 1 h) on the final properties of the coatings are analyzed. Second, the impact of using different silica precursors (TEOS:MTES) on the coating characteristics is examined.

3.1. Pore generator content effect on porous silica performance

In this section, the optical properties, thermal stability, microstructural properties and mechanical and environmental resistance are analyzed as a function of pore generator concentration in the solution.

The μ measurements showed no significant deviations remarking their long-term stability (see Fig. S3 of the supplementary data). It was also observed that the μ raised when the amount or concentration of Pluronic® was increased.

3.1.1. Optical characterization

A detailed study on the effect of Pluronic® concentration on the optical properties for concentrations up to 2.5 % v/v was conducted. Since concentrations exceeding 2.5 % v/v did not yield further improvements in optical transmittance (see Fig. S1 of the supplementary information for details), they were excluded from the main investigation. In order to achieve maximum transmission around 600 nm, which is the λ zone with the maximum solar irradiance, it was necessary to optimize the coating thickness by adjusting the withdrawal rate in the

dip-coating process for each solution. As shown in Table 2, the r_w was systematically reduced from 26 to 18 cm/min as the Pluronic® concentration increased. This adjustment was necessary to compensate for the higher viscosity of the solutions. Fig. 3 illustrates the transmission spectra for varying concentrations of Pluronic®, each calibrated to achieve optimal transmittance around 600 nm, while Table 2 summarizes the hemispherical transmittance values at this λ, the τ_s and the withdrawal rate used for each pore generator concentration. The correlation between the adjusted r_w and the optical performance confirms that the target thickness was precisely achieved for all formulations, centering the maximum transmittance at the desired wavelength.

The results summarized in Table 2 demonstrate a clear trend in the maximum transmittance values at 600 nm, highlighting the influence of Pluronic® concentration on the optical performance of the AR coatings. The transmittance increases progressively with higher concentrations of Pluronic®, reaching a maximum value of 99.8 % for the P-2.5 coating, an increase of 7.8 % over bare borosilicate. As noted in Table 2, τ_s values also increase by increasing the pore generator content, reaching a maximum of 0.976.

The calculated n spectrum of the AR coatings decreases systematically with increasing Pluronic® concentration, as shown in Fig. 4. This trend reflects the progressive increase in porosity induced by higher surfactant content, which lowers the effective refractive index of the films (see Table 3). A similar approach has been reported in previous studies. Agustín-Sáenz et al. [34] systematically varied the concentration of Pluronic® F-127 in a sol–gel synthesis of mesoporous silica coatings and demonstrated that increasing surfactant content led to higher porosity, which in turn reduced the refractive index and improved broadband antireflective performance for photovoltaic applications. Likewise, Meng et al. [54] investigated the effect of changing the amount of CTAB, a cationic surfactant, during the fabrication of silica-based coatings. They found that adjusting the surfactant concentration directly influenced surface morphology and porosity, enabling control over the refractive index and resulting in coatings with both excellent antireflective properties and mechanical robustness.

The values of n obtained at 600 nm are also indicated in Fig. 4. An n value as low as 1.215 was obtained for 2.5 %v/v Pluronic® concentration. Hemispherical reflectance measurements of the AR coated silicon wafers, presented in Fig. S4 of the supplementary data.

The porosity was calculated using the Eq. (6). Instead of using the theoretical value for a completely non-porous silica layer, it was considered as the non-porous reference the value obtained for the coating prepared without Pluronic® in the solution, even though sol–gel derived layers are known to exhibit a certain degree of intrinsic porosity. The calculated porosity values, together with the refractive index at 600 nm and coating thickness, both obtained by ellipsometry, are summarized in Table 2. The data demonstrate a clear trend where increasing Pluronic® concentration leads to higher porosity, and then lower refractive index. Porous SiO_2 coatings with 56 % of porosity were achieved by adding 2.5 % of Pluronic® to the precursor solution, finding the very low refractive index value required for producing the destructive optical interference on glass. The calculated thicknesses values for concentrations of 1.5, 2, and 2.5 are close to the desired theoretical value obtained by Eq. (2) (122 nm). The lower coating thickness values obtained for lower Pluronic® concentration also fit with the shift of the reflectance minimum towards shorter λ observed in Fig. 4b.

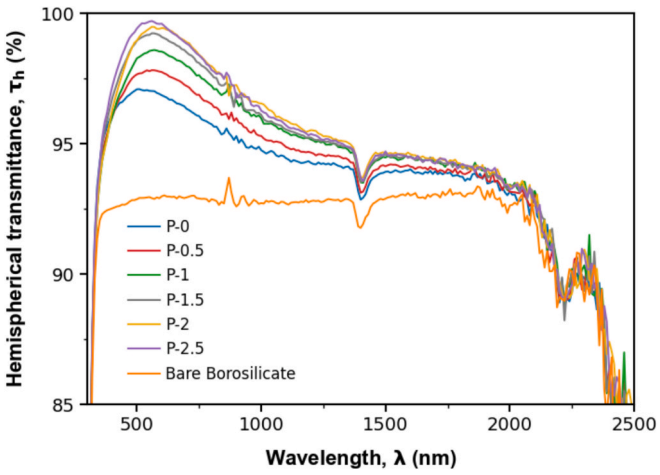

Fig. 3. Hemispherical transmittance spectra of anti-reflective coatings with varying Pluronic® concentrations (P-0 to P-2.5) compared to that of bare borosilicate glass.

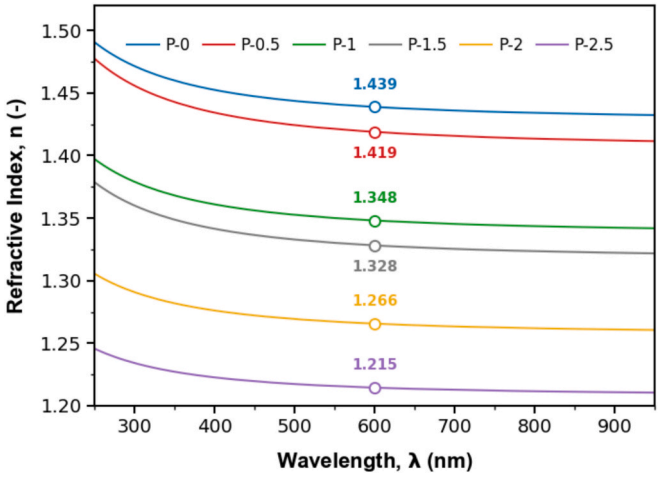

Fig. 4. Refractive index spectra (n) of the anti-reflective coatings deposited using different Pluronic® concentration obtained by fitting the ellipsometry data to the Cauchy model. The value of n at 600 nm is noted for every anti-reflective coating.

Table 3
Summary of the coating thickness, refractive index at 600 nm, and porosity for anti-reflective coatings prepared with varying concentrations of Pluronic®.

Pluronic® (% v/v)	0	0.5	1.0	1.5	2.0	2.5
***d* (nm)**	66.5	67.6	89.5	133.6	142.1	134.5
***n* @ 600 nm**	1.439	1.419	1.348	1.328	1.266	1.215
Porosity (%)	0	5	24	29	44	56

3.1.2. *Thermal analysis*

Thermogravimetric analysis was employed to gather information of the precursors' transformation happening during the heat treatment

Table 2
Spectral hemispherical transmittance values at 600 nm, calculated solar transmittance and withdrawal rate used for antireflective anti-reflective coatings with varying Pluronic® concentrations (P-0 to P-2.5) in comparison with bare borosilicate.

	P-0	P-0.5	P-1	P-1.5	P-2	P-2.5	Borosilicate
$\tau_{\lambda,h}$ (−)	0.969	0.976	0.986	0.992	0.995	0.998	0.927
τ_s (−)	0.951	0.955	0.959	0.968	0.974	0.976	0.924
Withdrawal rate (cm/min)	26	26	26	25	23	18	–

process and the effect of varying the pore generator concentration. From the TGA curves, we are able to identify the distinct stages of weight loss, reflecting the decomposition of organic and inorganic components [55].

In Fig. 5, the TGA curves of P-0 and P-2.5 samples, maintaining the silica precursors (MTES: TEOS) ratio at 50:50, are compared to evaluate the influence of Pluronic® on weight loss. To further analyze the weight loss behavior, the data were divided into four distinct temperature ranges and calculated the mass loss associated with each range. The resulting weight loss data, including the total mass loss for both solutions, are summarized in Table 4.

In the first zone (25–150 °C) different behaviour was obtained for the two powders. Both samples exhibit an initial weight loss at temperatures below 50 °C, which can be attributed to the evaporation of adsorbed water and low-boiling organic compounds [27]. For P-2.5 this weight loss is limited (4.1 %), progressing gradually up to ~ 150 °C, corresponding to the removal of physiosorbed water and residual ethanol trapped in the matrix. Whereas P-0, undergoes gradual mass losses of 30.9 % that are associated with the condensation of silanol groups (Si–OH to form Si–O–Si), releasing water as a by-product also described by Purcar et al. [56].

In the second zone (150–350 °C), P-2.5 experiences a sharp mass loss of 51.3 % centered at ~ 225–250 °C, clearly visible in the curve as an abrupt drop. This corresponds to the oxidative decomposition of the Pluronic® surfactant confined in the silica framework. For instance, Nguyen-Quang et al. [57] observed that increasing the concentration of Pluronic® in sol–gel silica systems leads to greater mass loss in the 150–300 °C range, directly associated with the thermal decomposition of surfactant residues. Bérubé et al. [58] observed that the degradation of Pluronic® occurs between 300 and 380 °C, with a pronounced peak around 310 °C, whereas Kleitz et al. [59] reported distinct weight losses at ~ 300 °C, associated with surfactant decomposition. Also Taromi et al. notice a sharp weight loss peak at 210 °C associated with the polymeric decomposition of Pluronic® [60]. In contrast, P-0 showed a weight loss of 9.1 % corresponding to the fraction that remained unreacted and is attributed to the decomposition of residual ethoxy/methoxy groups and the water released during silanol condensation, as reported in previous studies [61].

At higher temperatures, between 350 and 700 °C, thermal decomposition of both samples continues, although to different extents. For P-0, additional weight losses of 6.6 % and 5.1 % are attributed to the thermal decomposition and oxidation of organic moieties (–CH_3 groups) still functionalized on the silica surface, in agreement with previous reports [38]. In P-2.5, minor losses of 3.7 % and 1.8 % correspond to the combustion of carbonaceous residues from the surfactant and further condensation of the silica network. Above 600 °C, both samples reach a thermally stable phase, characterized by minimal further weight loss.

Table 4
Mass losses for several temperature ranges recorded by thermogravimetry for P-0 and P-2.5 (variation of surfactant concentration).

Pluronic® conc. (% wt)	25–150 °C (%)	150–350 °C (%)	350–500 °C (%)	500–700 °C (%)	Total mass loss (%)
0	30.9	9.1	6.6	5.1	51.7
2.5	4.1	51.3	3.7	1.8	60.9

However, P-0 retains a higher residual weight than P-2.5, reflecting the stabilizing effect of the non-porous, surfactant-free matrix. This highlights the trade-off between porosity and thermal stability in hybrid silica systems: while Pluronic® incorporation increases porosity and enhances optical performance, it introduces thermal vulnerability due to the higher organic content and structural porosity.

Overall, these results confirm that Pluronic® leaves a distinct thermal signature, with a dominant decomposition step at ~ 275–300 °C, while samples synthesized without the surfactant exhibit progressive weight loss dominated by solvent evaporation, silanol condensation, and decomposition of methyl/ethoxy groups from the alkoxysilanes. This analysis underscores the delicate balance between structural porosity and thermal stability in hybrid silica material.

Fig. 6 presents the DTA profiles for the P-0 and P-2.5 samples. The thermal profiles of the samples display the typical behavior of hybrid silica systems derived from TEOS and MTES. A pronounced exothermic peak appears between approximately 250 and 300 °C in the sample containing Pluronic®, which is attributed to the oxidative decomposition of the template confined in the inorganic network. Mirtaheri et al. [62], reported a similar exothermic event at 280 °C, which was attributed to the combustion of the Pluronic® copolymer within mesoporous tungsten oxide. Below 200 °C, both samples exhibit a slight endothermic deviation associated with the loss of adsorbed water and residual solvents, in agreement with observations made by Dudás et al. [63]. Finally, a minor thermal signal around 600 °C can be attributed to the revealing the onset of new population of –CH_3 inside the solution structure [63].

3.1.3. Surface morphology

The textural properties of the coatings were analyzed through nitrogen physisorption isotherms to evaluate the effect of Pluronic® concentration on porosity and surface area. The sorption isotherms obtained for all samples exhibit Type Ib behavior, typical for materials having wider micropores and narrow mesopores, as shown in Fig. 7a. According to the IUPAC classification, Type Ib isotherms are

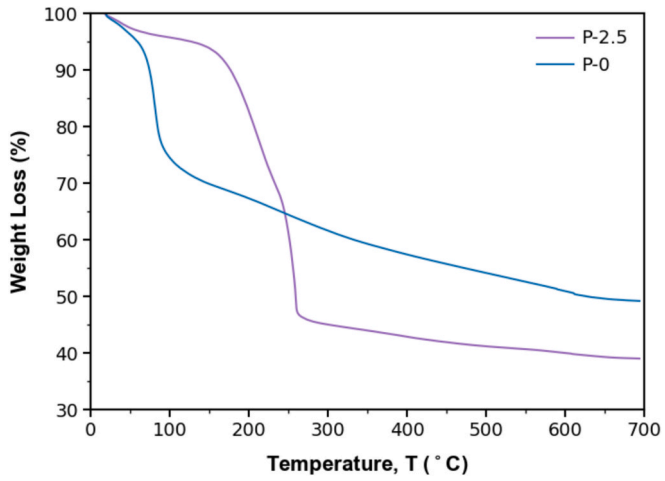

Fig. 5. Comparison of thermogravimetric curves of P-0 and P-2.5 powders.

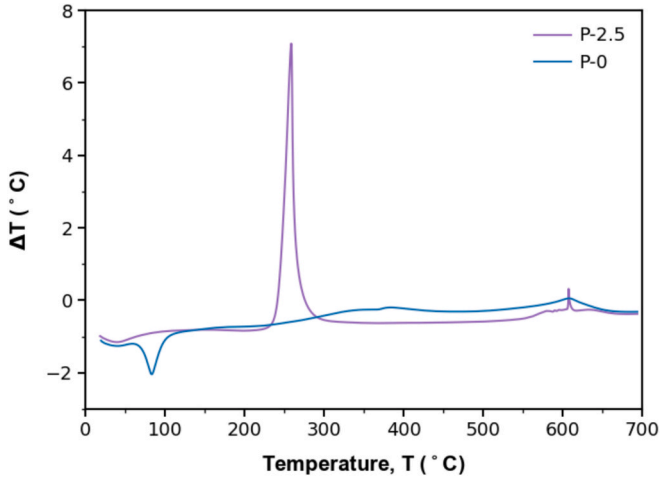

Fig. 6. Differential thermal analysis curves for samples P-0 and P-2.5.

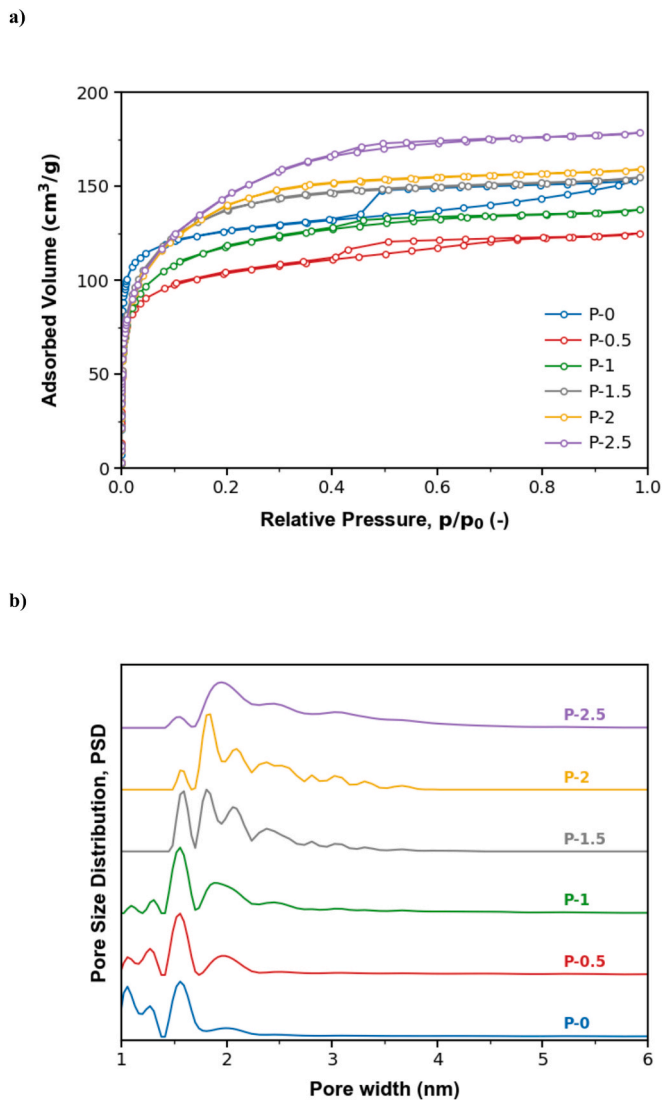

Fig. 7. a) Nitrogen sorption isotherms and b) pore size distributions for samples P-0 to P-2.5.

characteristic of microporous and mesoporous materials [64], which is in accordance with broader pore size distributions (Fig. 7b), showing the presence of micropores and mesopores in all samples.

As summarized in Table 5, S_{BET}, total pore volume (V_t), and pore diameter as the maximum of the pore size distribution (Fig. 7b) (w_{max}) exhibit systematic variations as a function of Pluronic® concentration. A clear correlation is observed between Pluronic® content and the resulting porous properties. As the porosity generator content increases (except for P-0.5), also the surface area and total pore volume is increased, reaching a maximum of 510 m^2/g and 0.275 cm^3/g for P-2.5. Samples from P-0 to P-1 show micropores and mesopores in the range of 1.0 to 3.2 nm, with maxima from 1.55 to 1.56 nm. In contrast, larger mesopores are observed for samples P-1.5 and P-2 to P-2.5, with maxima at 1.81, 1.86, and 1.96 nm, respectively. It can be seen that the pore size

Table 5
Textural parameters of the samples determined from the nitrogen adsorption isotherms, influenced by varying the Pluronic® content.

Pluronic® (% v/v)	0	0.5	1	1.5	2	2.5
S_{BET} (m^2/g)	395	331	367	437	458	510
V_t (cm^3/g)	0.233	0.192	0.211	0.237	0.245	0.275
w_{max} (nm)	1.55	1.55	1.56	1.81	1.85	1.96

of the samples increases with higher surfactant content. This trend reinforces the templating role of Pluronic® in promoting mesoporous formation, consistent with previous studies on surfactant-assisted sol–gel processes. Moreover, the gradual increase in pore size distribution with higher Pluronic® content further supports the role of the surfactant in modulating the final mesoporous architecture [65].

A notable deviation is observed in the case of P-0, which, despite the absence of a pore-generating agent, exhibits a relatively high surface area (395 m^2/g). This apparent porosity can be attributed to the formation of interparticle voids and irregular intraparticle pores, resulting from the rapid and untemplated condensation of the TEOS:MTES network. Such behavior is consistent with observations reported by Dudás et al. [63] for xerogels with ~ 60 % MTES, where porosity was detected even in the absence of surfactants. Upon the introduction of low Pluronic® concentrations (0.5–1 % v/v), a slight decrease in S_{BET} and V_t is observed (331–367 m^2/g and 0.192–0.211 cm^3/g, respectively), likely due to partial disruption of the interparticle voids before the formation of well-defined micropores. At higher concentrations (1.5–2.5 % v/v), Pluronic® effectively directs the formation of ordered micropores, leading to a progressive increase in S_{BET}, V_t, and w_{max} of 1.96 nm. These results indicate that, although P-0 exhibits a high apparent pore size, this porosity does not contribute significantly to optical properties, whereas the mesopores templated by Pluronic® are responsible for improved optical and structural performance.

The data obtained for samples with 3.3 % v/v showed higher S_{BET}, V_t and w_{max} (see Figure S2 of the Supplementary data). The formation of mesopores is further corroborated by the observed hysteresis loops. The progressive increase in nitrogen uptake at higher relative pressures, particularly in samples with higher Pluronic® content, reinforces the hypothesis of improved pore interconnectivity, as reported in other templated silica systems [66]. The correlation between porosity and durability will be further explored in subsequent sections, particularly in relation to mechanical and environmental stability.

SEM images (Fig. 8) of sample P-0 (a) show a dense and uniform silica layer with no visible porosity. In contrast, sample P-2.5 (b) exhibits a significant porous structure. The formation of porous follows the expected trend of increasing pore size and density with higher concentrations of the pore-generating agent.

The comparison of nitrogen adsorption data with SEM images of P-0 and P-2.5 supports the hypothesis that the apparent porosity in P-0 arises from interparticle voids, whereas the well-defined micropores in P-2.5 result from Pluronic® templating.

In Fig. 9, the porosity calculated together with the surface static contact angle of the AR coatings is represented. The relationship between porosity and wettability is evident in the observed decrease in WCA with increasing Pluronic® concentration. Higher porosity, driven by greater surfactant content, enhances surface hydrophilicity by increasing the effective surface area and facilitating water spreading. This trend is consistent with findings from Buijnsters et al. [67], who reported a sharp reduction in WCA as porosity increased in anodized aluminum oxide films, transitioning the surface from hydrophobic to hydrophilic behavior. Similarly, Norek et al. [68] observed that porosity beyond 50 % significantly lowered WCA due to enhanced surface interactions with water. This effect aligns with the role of surfactants in modifying surface energy, as described by Meng et al. [69], where higher surfactant concentrations decreased WCA by promoting hydrophilic interactions. Therefore, the increase in porosity in the coating, necessary to increase the glass transmittance, implies a more reactive surface and susceptible to the adherence of dust and/or contaminant species.

3.1.4. Mechanical and environmental durability

To investigate the impact of annealing duration on the durability and environmental resistance of the coatings, P-0 to P-2.5 samples were sintered at 500 °C for 15 min and 1 h. The abrasion resistance of the samples was tested and R_a was subsequently characterized via

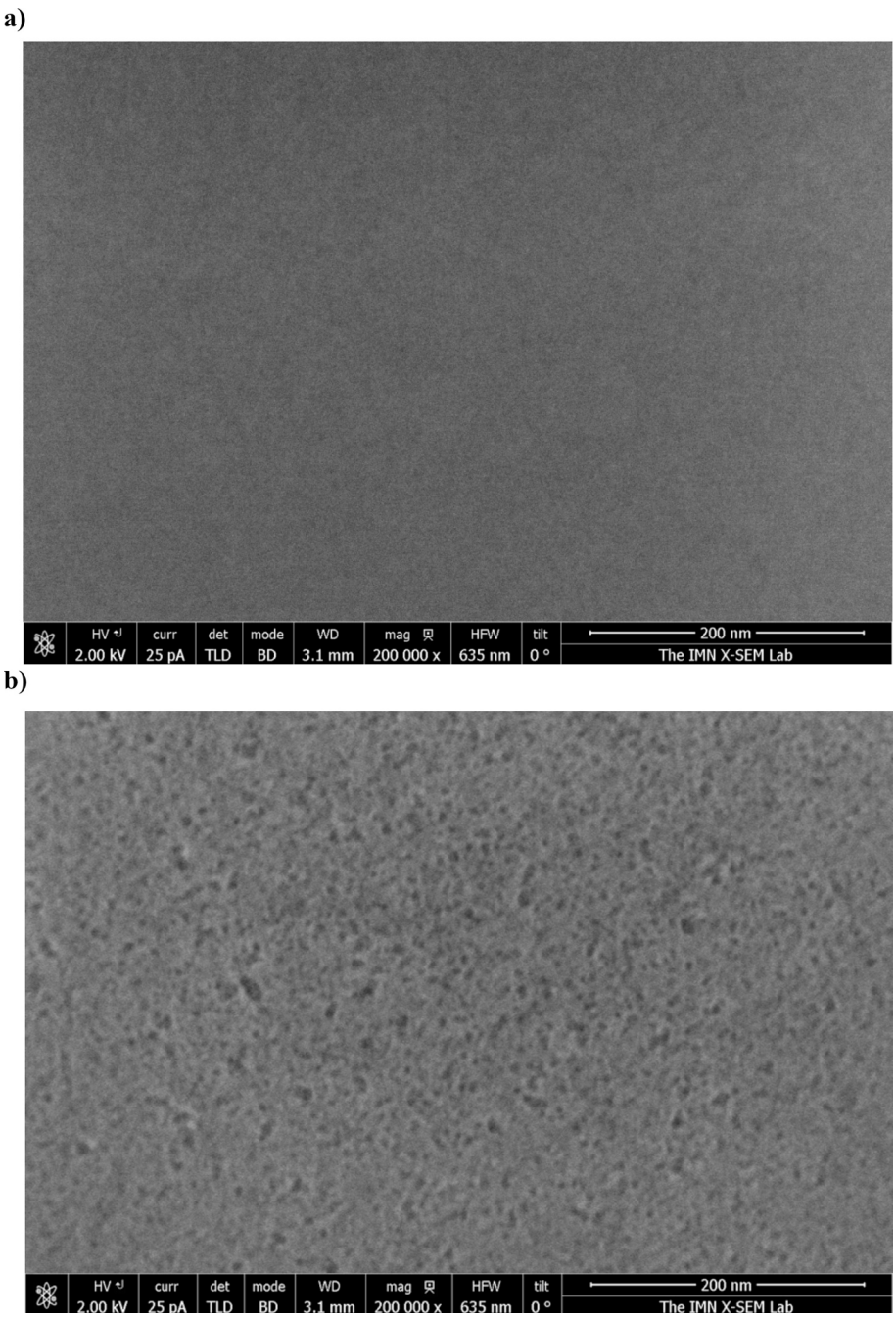

Fig. 8. Scanning electron microscope images for P-0 (a) and P-2.5 (b).

profilometry after certain accumulative abrasion cycles. Fig. 10 presents the resulting data for the 15-minute anneal (a) and the 1-hour anneal (b). Initially, the coatings exhibit low roughness values; as the number of abrasion cycles increases, the roughness rises due to the accumulation of scratches. At more advanced stages, the roughness decreases again because larger portions of the coating are removed, eventually exposing the underlying smooth glass. Samples treated thermally for 15 min (Fig. 10a) display higher abrasion resistance compared to those sintered for 1 h (Fig. 10b), as they presented lower R_a values which indicate the scratches at higher number of cycles. This effect may be attributed to the more extensive burnout of the organic matter and pore-forming agent during prolonged heating, resulting in a more fragile, weaker and porous structure that is less able to withstand mechanical stress. Similarly, as Pluronic® concentration increases, the abrasion resistance decreases. This trend can be attributed to the higher porosity introduced by greater amount of Pluronic®, which, when burned off during thermal treatment, creates a more open and mechanically weaker silica network. These results are consistent with those reported by Kessman et al. [70], who demonstrated that increasing the concentration of the porogen template in mesoporous silica coatings leads to higher porosity, which in turn reduces the mechanical robustness under abrasion and tribological tests.

In addition to tracking the evolution of R_a with the number of abrasion cycles, the τ_s values of the sintered samples were calculated and are presented in Fig. 11. The error bars represent the standard deviation of three measurements in each sample. As it is observed, the initial τ_s values are almost identical for both heat treatments. In the case of the samples sintered for 1 h (Fig. 11b), the loss in τ_s is more evident at low abrasion cycles in agreement with the roughness measurements when compared with the samples sintered for 15 min (Fig. 11a). The only sample that does not follow this behavior is P-0, which, as previously

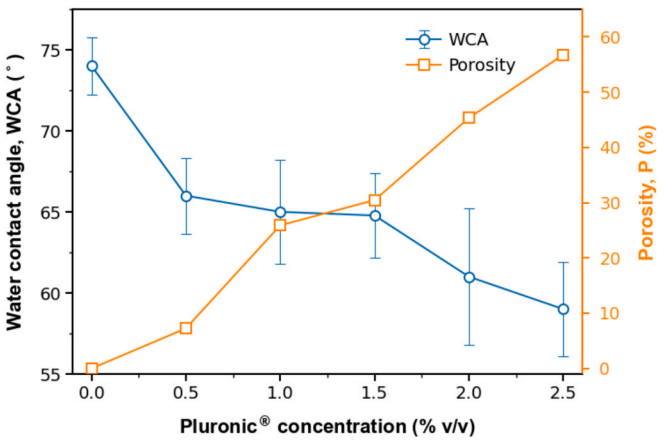

Fig. 9. Correlation between Pluronic® concentration with water contact angle and porosity.

discussed, does not contain the pore-forming agent Pluronic®. As a result, it forms a dense silica network in which longer sintering times promote stronger film adhesion, in line with what has been reported in earlier studies [71]. It should also be noted that the transmittance values do not reach that of bare glass (0.92), since the substrate is coated on both sides.

Fig. 12 presents optical microscopy images of selected coatings (P-1, P-1.5, and P-2.5) at different abrasion stages (initial, 20, 50, and 150 cycles). The upper rows (Fig. 12a) correspond to samples sintered at 500 °C for 15 min, while the lower rows (Fig. 12b) represent those sintered for 1 h. These samples were chosen as representative cases to illustrate the impact of both thermal treatment duration and Pluronic® concentration on surface degradation, though all compositions were systematically evaluated.

The effect of thermal treatment time is evident when comparing the same formulation under different sintering durations. For both P-1 and P-1.5, the 15-minute sintered sample exhibits gradual surface wear, with visible scratches appearing after 50 cycles, and some coating residue remaining after 150 cycles. However, after 1 h of sintering, the coating becomes significantly more brittle, showing deeper and more widespread cracks, with the glass already visible in some areas after 20 abrasion cycles, and exhibiting notable material detachment beyond 50 cycles. No presence of coating remains after 150 cycles. The most severe degradation is observed in P-2.5, which contains the highest Pluronic® concentration. In the 15-minute sintered sample, initial defects emerge at 20 cycles, progressing to widespread material loss at 50 cycles, consistent with the increased porosity observed in nitrogen adsorption measurements. The 1-hour sintered counterpart exhibits even lower stability, with rapid degradation occurring as early as 20 cycles, leading to near-complete failure at 50 cycles.

This behavior is consistent with the roughness measurements presented in Fig. 10, where increased sintering time and higher Pluronic® content were directly linked to greater surface degradation. This degradation is attributed to the higher porosity introduced by the surfactant, which weakens the silica network and makes it more prone to mechanical failure when subjected to prolonged thermal exposure.

To gain further insight into the mechanical performance of the coatings, pencil hardness tests were also conducted. The results obtained are summarized in Table 6.

A marked decrease in hardness is observed as the amount of pore-forming agent increases, for both sintering temperatures. When

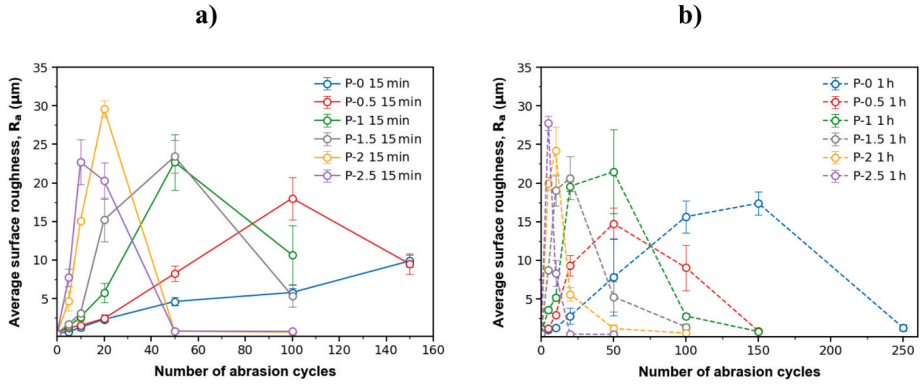

Fig. 10. Average surface roughness evolution of coatings with varying Pluronic® concentrations (P-0 to P-2.5) after different thermal treatment durations as a function of the number of abrasion cycles: a) 15 min of heat treatment and b) 1 h of heat treatment.

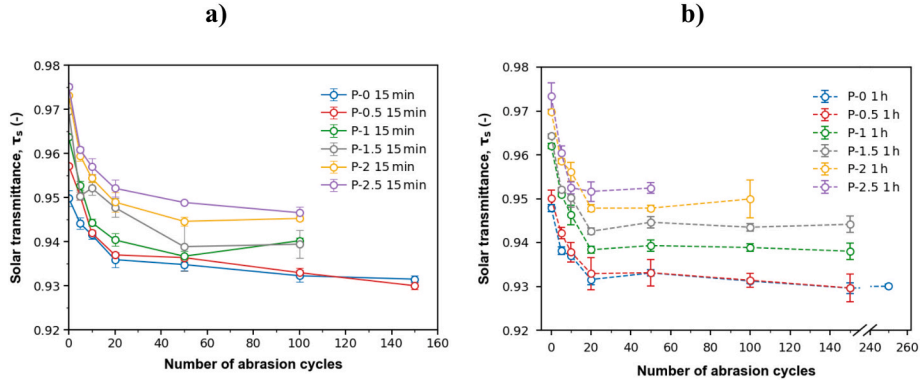

Fig. 11. Solar transmittance values of AR coating varying Pluronic® concentrations (P-0 to P-2.5) thermally treated for different times as function of the number of abrasion cycles: a) 15 min heat treatment and b) 1 h heat treatment.

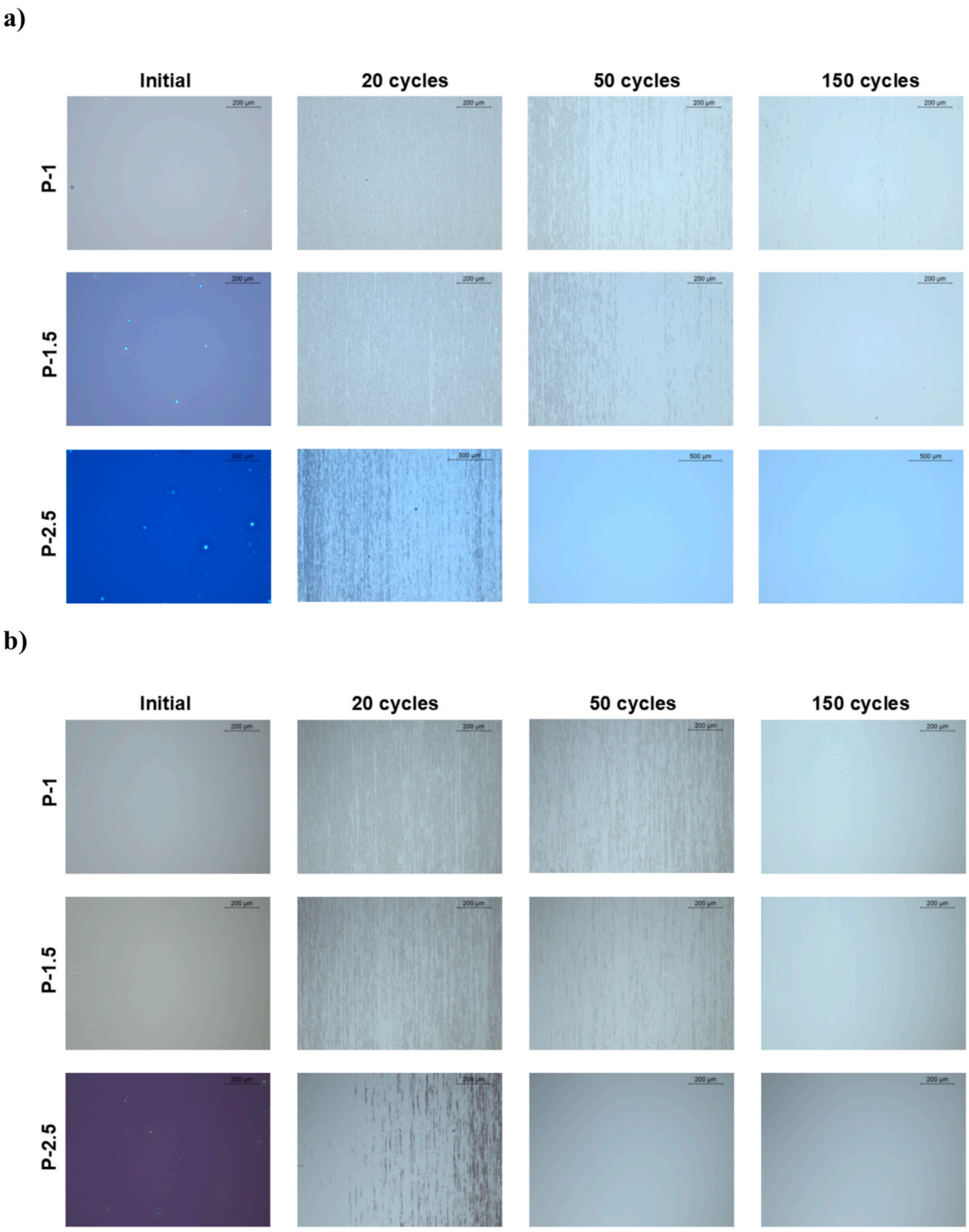

Fig. 12. Optical microscopy images of selected coatings (P-1, P-1.5, and P-2.5) before and after abrasion testing at different cycle stages (initial, 20, 50, and 150 cycles). (a) Samples sintered at 500 °C for 15 min and (b) Samples sintered at 500 °C for 1 h.

comparing different sintering times, a reduction in hardness is also evident in the samples treated for longer periods. In contrast, for the samples without Pluronic® (P-0), the opposite trend is observed: longer sintering times lead to higher hardness values. Results from pencil hardness test matches results obtained from abrasion resistance (see Fig. 11).

Next, the evaluation of the weathering resistance of coatings is presented. It should be noted that for the condensation tests and combined UV radiation and condensation cycles, the samples sintered for 15 min were coated on one side, while those sintered for 1 h were coated on both sides of the substrate and this explains the differences in the initial τ_s values. The results of τ_s and WCA variations during the condensation aging test for samples sintered for 15 min and 1 h are shown in Fig. 13, Table 7 and Table 8.

Table 6
Results obtained from hardness pencil test for coatings with varying Pluronic® concentrations (P-0 to P-2.5) after 15 min and 1 h thermal treatment.

Pluronic® conc. (% wt)	15 min sintering time	1 h sintering time
0	H	2H
0.5	HB	B
1	B	2B
1.5	5B	4B
2	6B	>6B
2.5	>6B	>6B

Under continuous condensation exposure, a slight decline in τ_s was observed across all samples during the 480 h test. Regarding the evolution of τ_s in the samples sintered for 15 min, they did not follow a perfectly linear trend with Pluronic® concentration. In general, τ_s shows a small drop in the first hundred hours followed by a very small decrease in transmittance until the end of the test. The total decrease ranges from 0.32 % to 1.68 %. Water adsorption within the pore network increases the effective refractive index and thereby reduces τ_s, as reported for nanoporous AR coatings [72]. In that context, moisture-induced transmission variations around ~ 1 percentage point are commonly observed as small, reversible effects in stable mesoporous systems [72]. Coatings sintered for 1 h displayed a highly stable behavior during the 480 h condensation test. The sample P-0 showed a minor decrease in τ_s of 0.53 %, while P-0.5 and P-1 exhibited slightly higher changes of 0.84 % and 0.94 %, respectively. The samples with higher surfactant content (P-1.5, P-2, and P-2.5) showed similarly low variations between 0.7 % and 1.2 %, indicating no clear correlation with Pluronic® concentration. Nevertheless, it is important to remark that very small variations in τ_s were observed, highlighting the stability of the AR coatings against condensation. However, substantial changes in the WCA values were seen during the test. For the samples sintered for 15 min, the sample without Pluronic® showed the largest drop in WCA, from 74° to 39°, indicating that the surface became considerably more hydrophilic after exposure. This behavior can be attributed to the limited condensation of silanol groups during the short thermal treatment, leaving a high density of hydrolysable Si–OH species. Exposure to humidity promotes their rehydration and the regeneration of additional silanol sites, consistent with previous studies on hybrid coatings aged under moisture [73]. In the coatings containing Pluronic®, the evolution of WCA did not follow a clear linear trend. Although all coatings containing Pluronic® showed a decrease in contact angle after ageing, the magnitude of this change varied with surfactant concentration. The sample with P-1.5 showed the largest reduction, from 56° to 21° (62.5 %), whereas other formulations exhibited moderate losses, ranging from 33.9 % for P-1 to 46.8 % for P-0. These results suggest that the effect of Pluronic® on surface wettability is complex and arises from competing phenomena. For the samples sintered for 1 h, the decline in τ_s and WCA was smaller than in the 15 min samples. The sample P-0 showed a decrease in WCA from 74° to 49° (33.8 %), while P-0.5, P-1, P-1.5, and P-2 displayed progressively larger

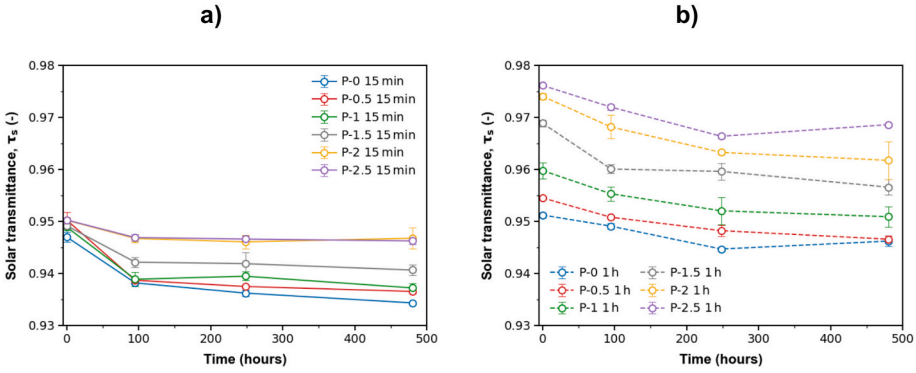

Fig. 13. Evolution of calculated solar transmittance of coatings with varying Pluronic® concentrations (P-0 to P-2.5) as a function of condensation exposure test time: a) samples sintered for 15 min and b) sintered for 1 h.

Table 7
Water contact angle and calculated solar transmittance measured for samples sintered for 15 min before, during and after condensation for 480 h.

Pluronic® conc. (% wt)	τ_s before exposure	τ_s after 95 h exposure	τ_s after 248 h exposure	τ_s after exposure (480 h)	Change (%)	WCA before exposure	WCA after exposure (480 h)	Change (%)
0	0.947	0.938	0.936	0.934	1.37	74	39	47.3
0.5	0.948	0.939	0.937	0.937	1.68	62	33	46.8
1	0.949	0.940	0.939	0.938	1.16	56	37	33.9
1.5	0.949	0.942	0.942	0.941	0.84	56	21	62.5
2	0.950	0.948	0.947	0.947	0.32	54	32	40.7
2.5	0.951	0.947	0.947	0.947	0.42	51	29	37.3

Table 8
Water contact angle and calculated solar transmittance measured for samples sintered for 1 h before, during and after condensation for 480 h.

Pluronic® conc. (% wt)	τ_s before exposure	τ_s after 95 h exposure	τ_s after 248 h exposure	τ_s after exposure (480 h)	Change (%)	WCA before exposure	WCA after exposure (480 h)	Change (%)
0	0.951	0.949	0.945	0.946	0.53	74	49	33.8
0.5	0.955	0.951	0.948	0.947	0.84	66	37	44.0
1	0.960	0.955	0.952	0.951	0.94	66	36	45.5
1.5	0.969	0.968	0.963	0.962	0.72	66	25	63.1
2	0.974	0.968	0.963	0.962	1.23	61	21	65.6
2.5	0.976	0.972	0.966	0.969	0.72	59	22	62.7

reductions of 44.0 %, 45.5 %, 63.1 %, and 65.6 %, respectively. Only the sample P-2.5 slightly deviated from this trend, with a loss of 62.7 %. This suggests that despite the higher condensation of the silica network achieved during the longer heat treatment, the surface of the templated films remained sensitive to water adsorption and rehydroxylation (Table 9).

When compared with the results obtained under condensation alone, the combined UV and condensation exposure produced slightly smaller variations in τ_s but a more defined trend in surface wettability. In all cases, the overall optical degradation remained below 2 %, confirming the excellent transparency and structural stability of the hybrid silica network. However, while the 15 min coatings exposed only to humidity showed no clear relationship between WCA loss and surfactant concentration, the addition of UV irradiation led to a progressive decrease in hydrophobicity with increasing Pluronic® content. This behavior suggests that the organic moieties present in the hybrid matrix, particularly the methyl groups from the residual carbon species associated with Pluronic®, are more susceptible to photo-oxidation. In addition, for 1 h sintered samples, the evolution of surface wettability also showed smaller changes than in the condensation test. The WCA losses decreased from 33 to 66 % under condensation to 11–50 % under combined UV radiation and condensation (Table 10).

When considering all climatic aging results, the coatings showed a consistent response to both humidity and UV exposure. The most significant changes in WCA and τ_s occurred during the condensation test, regardless of sintering time, indicating that prolonged exposure to continuous moisture is the dominant degradation mechanism for these AR coatings. In contrast, during the combined UV and condensation test, the overall variations were smaller, and the coatings maintained high optical stability (< 1.5 %). This difference can be directly related to the test conditions. The reduced time under constant condensation significantly limited the rehydroxylation of the surface and the adsorption of water within the porous network, explaining the smaller WCA and τ_s variations. Moreover, UV radiation did not introduce any measurable optical degradation, confirming the strong photochemical stability of the silica-based framework (Fig. 14).

3.2. *Influence of the TEOS: MTES composition ratio on porous silica properties*

In this section, the amount of Pluronic® was kept constant at 2.5 % v/v while varying the proportions of the silica precursors TEOS and MTES in ratios of 50:50, 70:30, and 90:10. The heat treatment time was 15 min for all the samples. Once more, the stability of the precursors

Table 9
Water contact angle and calculated solar transmittance measured for samples sintered for 15 min before, during and after combination of UV radiation and condensation for 480 h.

Pluronic® conc. (% wt)	τ_s before exposure	τ_s after 182 h exposure	τ_s after 343 h exposure	τ_s after exposure (480 h)	Change (%)	WCA before exposure	WCA after exposure (480 h)	Change (%)
0	0.947	0.942	0.942	0.943	0.42	73	65	10.9
0.5	0.948	0.937	0.935	0.938	1.05	62	42	32.3
1	0.949	0.934	0.931	0.934	1.46	61	36	41.0
1.5	0.949	0.932	0.930	0.934	1.46	56	31	44.6
2	0.949	0.941	0.940	0.941	0.93	56	26	53.6
2.5	0.950	0.941	0.940	0.940	0.21	54	26	50.0

Table 10
Water contact angle and calculated solar transmittance measured for samples sintered for 1 h before, during and after combination of UV radiation and condensation for 480 h.

Pluronic® conc. (% wt)	τ_s before exposure	τ_s after 182 h exposure	τ_s after 343 h exposure	τ_s after exposure (480 h)	Change (%)	WCA before exposure	WCA after exposure (480 h)	Change (%)
0	0.951	0.950	0.950	0.948	0.32	73	65	11.0
0.5	0.955	0.950	0.950	0.949	0.75	64	47	26.6
1	0.960	0.952	0.952	0.951	0.86	60	37	38.3
1.5	0.969	0.960	0.964	0.962	0.74	57	31	45.6
2	0.974	0.971	0.970	0.972	0.21	54	27	50.0
2.5	0.976	0.971	0.969	0.971	0.53	54	29	46.3

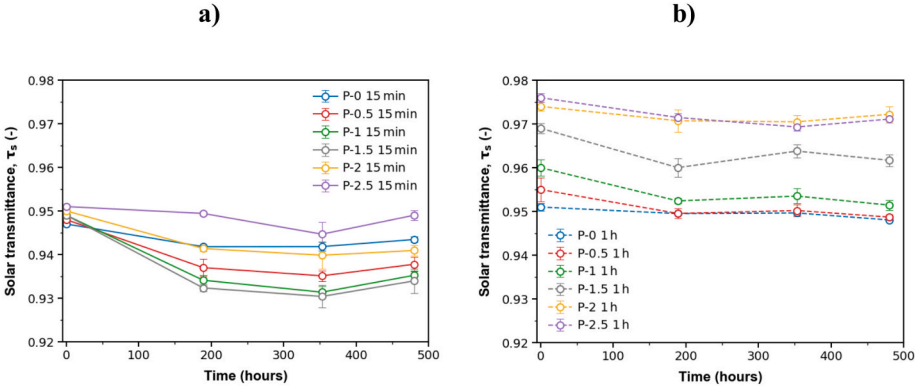

Fig. 14. Evolution of calculated solar transmittance of coatings with varying Pluronic® concentrations (P-0 to P-2.5) as a function of condensation time under UV radiation: a) samples sintered for 15 min and b) samples sintered for 1 h.

solutions was checked by measuring the viscosity over time. The solutions remain stable for a period of up to 252 days since no significant changes were observed (see Fig. S5 of the supplementary data). Also worth noting is that the gradual substitution of TEOS by MTES (ratios going from 9:1 to 5:5) led to more viscous solutions.

3.2.1. Optical characterization

Similar to the Pluronic® series, the withdrawal rate was optimized for each TEOS:MTES ratio to achieve maximum transmittance around 600 nm. As shown in Fig. S5, increasing the MTES content leads to a denser and more viscous solution, requiring a specific adjustment of r_w to compensate for these rheological changes. Although very high transmittance values were obtained for all three configurations (see Fig. 15), increasing the TEOS content from 50:50 (P-5:5) to 90:10 (P-9:1) resulted in a slight drop in transmittance, particularly in the visible and near-infrared ranges. Initial maximum transmittance values of 99.8 %, 99.5 % and 97.6 % were obtained for P-5:5. P-7:3 and P-9:1 respectively. These variations are explained with the increase of hydrophobicity of the surface and inner silica matrix due to the inclusion of methyl groups from MTES [63]. The more hydrophobic nature of P-5:5 makes the surface less reactive to the adsorption of humidity and/or water in the pores, maintaining the low refractive-index. This claim is also supported by WCA measurements, with the average WCA values obtained for P-5:5, P-7:3, and P-9:1 being 56°, 29° and 26° respectively.

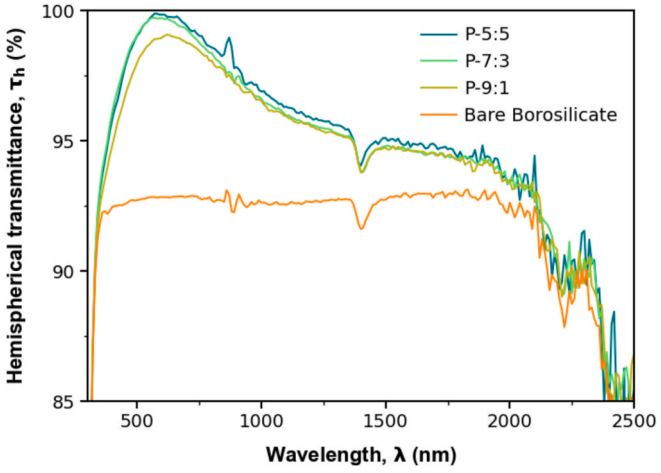

Fig. 15. Hemispherical transmittance spectra of anti-reflective coatings with varying TEOS:MTES ratios (50:50, 70:30, and 90:10).

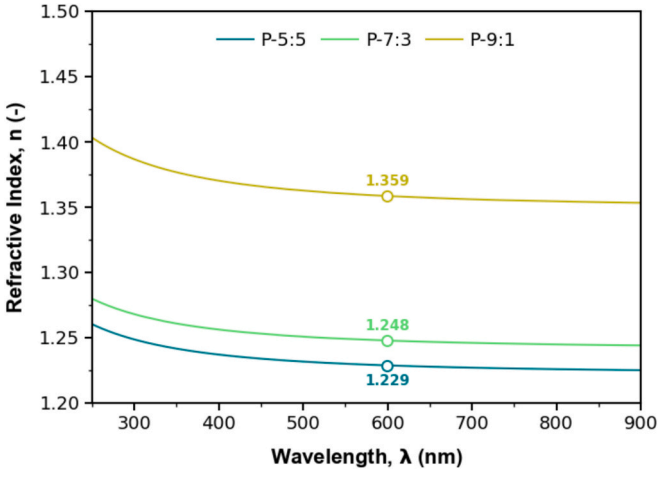

Fig. 16. Refractive index spectra of coatings with varying TEOS:MTES ratios (50:50, 70:30, and 90:10).

The transmittance spectra also correlate with the refractive index values obtained for these coatings, which are plotted in Fig. 16. As it is observed in the plot, P-9:1, with the highest TEOS content, exhibits the highest value (1.359 at 600 nm), reflecting its more reactive surface to the absorption. As the MTES content increases in P-7:3 and P-5:5, the refractive index decreases to 1.248 and 1.229, respectively, consistent with the more hydrophobic surface which avoids the absorption. The reflectance spectra on silicon wafers can be seen on the supplementary data on Fig. S6.

These results underline the combined impact of precursor ratios and surfactants on the optical properties of the coatings. Higher TEOS content increases network density and refractive index but reduces AR efficiency (Fig. 16).

Theoretical porosity calculations using Eq. (6) also confirms this trend. As can be seen in Fig. S7 in the supplementary data, by increasing MTES content, we obtain a less dense matrix and a lower refractive index. i.e. precursor composition can be directly related to the structural properties of the AR coating.

3.2.2. Thermal analysis

Thermogravimetric analysis was employed to examine the thermal degradation behavior of samples P-5:5 and P-9:1 (Fig. 17). The corresponding mass losses sections recorded by thermogravimetry are summarized in Table 11. Both samples exhibit an initial weight loss below 150 °C, attributed to the evaporation of adsorbed water and volatile organic species physically trapped in the silica matrix [27,60,74]. For P-5:5, this early mass loss (4.1 %) is moderate, indicating a relatively compact hybrid structure that limits water retention. In contrast, P-9:1 displays a slightly higher loss (8.2 %) in this range, suggesting an increased amount of physically adsorbed water and residual ethanol. Between 150 °C and 350 °C, the most significant decomposition event occurs for both samples, corresponding to the removal of the organic template and condensation of silanol groups. P-5:5 exhibits a major weight loss of 52.3 %, associated with the oxidative degradation of Pluronic® confined within the silica framework, along with the elimination of residual organic moieties derived from the MTES precursor

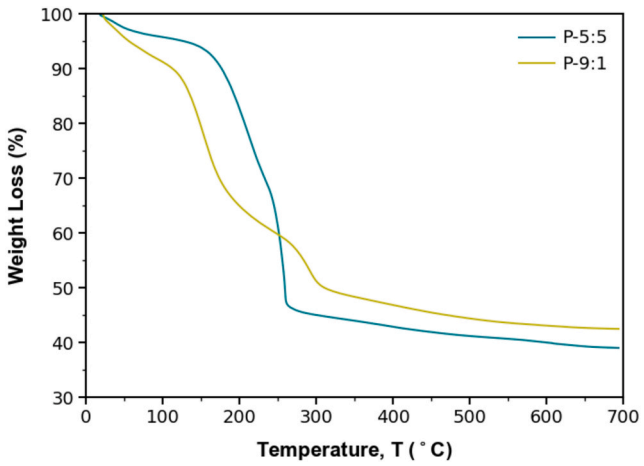

Fig. 17. Thermogravimetric analysis curves of anti-reflective samples. Comparison of P-5:5 and P-9:1 with varying MTES ratios.

Table 11
Mass losses recorded by thermogravimetry for P-5:5 and P-9:1 (variation of TEOS:MTES ratio).

TEOS:MTES ratio	25–150 °C (%)	150–350 °C (%)	350–500 °C (%)	500–700 °C (%)	Total mass loss (%)
50:50	4.1	52.3	2.7	1.8	60.9
90:10	8.2	44.0	3.0	2.4	57.6

[56]. On the other hand, P-9:1 shows a lower mass loss (44.0 %) in this region, indicating that a higher TEOS proportion leads to a denser matrix. This reduced mass loss suggests more efficient condensation and crosslinking of Si–O–Si bonds, as Dudás et al. [63] demonstrated. In the subsequent range from 350 to 700 °C, both samples continue to exhibit minor weight losses due to the oxidation of residual carbonaceous species and decomposition of remaining methyl groups (–CH_3) still bonded to the silica surface [58,75]. P-5:5 losses 4.5 % in this range, while P-9:1 shows a slightly higher 5.4 %. Overall, the total mass losses amount to 60.9 % for P-5:5 and 57.6 % for P-9:1.

Fig. 18 presents DTA profiles for samples P-9:1 and P-5:5, highlighting key thermal degradation stages and associated endothermic or exothermic reactions. Differences are observed in the peak associated to the oxidative decomposition of Pluronic® encapsulated within the silica matrix (250 °C – 350 °C zone). The intensity and sharpness of this peak are more pronounced in sample P-5:5, suggesting a more confined or ordered arrangement of the template within the network. This behavior aligns with observations made by Mirtaheri et al. [62], who attributed similar exothermic signals to the combustion of P-123 in mesostructured oxide frameworks. The slight shift observed in the main exothermic peak between P-5:5 and P-9:1 might be explained by structural differences induced by the TEOS:MTES ratio. According to Yu et al. [37] and Dudás et al. [63], increasing the MTES content reduces the degree of network condensation and enhances the presence of organic moieties, leading to an earlier decomposition of the template due to a more open and less cross-linked silica matrix.

3.2.3. Surface morphology

The textural and microstructural properties of the coatings were evaluated using nitrogen physisorption and SEM to investigate the influence of TEOS:MTES ratio on porosity development. The nitrogen adsorption–desorption isotherms, presented in Fig. 19a, also exhibit a Type Ib behavior. Pore size distributions are shown in Fig. 19b.

As summarized in Table 12, the S_{BET}, V_t, and w_{max} exhibit systematic but non-linear variations as a function of the TEOS:MTES ratio. The sample with a 50:50 composition shows a surface area of 510 m^2/g, a total pore volume of 0.275 cm^3/g, and a w_{max} of 1.96 nm. For the 70:30 sample, S_{BET} increases slightly to 541 m^2/g, with a corresponding V_t of 0.283 cm^3/g and a w_{max} of 1.90 nm. In the 90:10 sample, a surface area of 423 m^2/g is recorded, with V_t at 0.235 cm^3/g and w_{max} at 0.82 nm.

Similar non-linear trends have been reported in the literature. Dudás et al. [63] found that average pore diameter decreased progressively with increasing MTES up to 40 %, but unexpectedly increased again at 60 %, coinciding with a sharp growth in primary particle diameter. In their work, they attribute this behavior to changes in the material structure resulting from the incorporation of –CH_3 groups and the consequent reduction of cross-linking density upon MTES addition. Likewise, Zhao et al. [76] observed that while porosity and pore volume peaked at TEOS:MTES = 0.75, further increase to a ratio of 1.5 led to a significant decline, indicating a threshold beyond which excessive methylation compromises mesopore formation. Putz et al. [77] also observed an anomalous trend in the evolution of textural properties with TEOS:MTES ratio, where the specific surface area increased up to an intermediate composition and then decreased at higher MTES contents. They attributed this behavior to partial occlusion of the pore channels as surface hydroxyl groups are progressively replaced by methyl groups.

These trends are further validated by SEM analysis. As shown in Fig. 20, both P-5:5 and P-9:1 samples exhibit a homogeneous

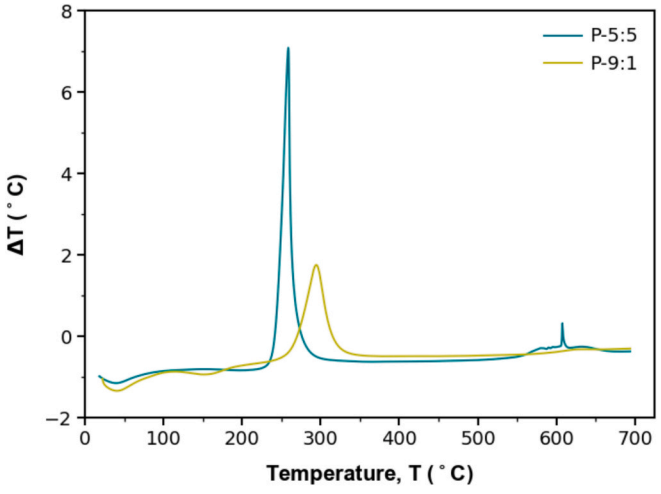

Fig. 18. Differential thermal analysis curves of anti-reflective samples showing weight loss and thermal events: P-9:1 and P-5:5.

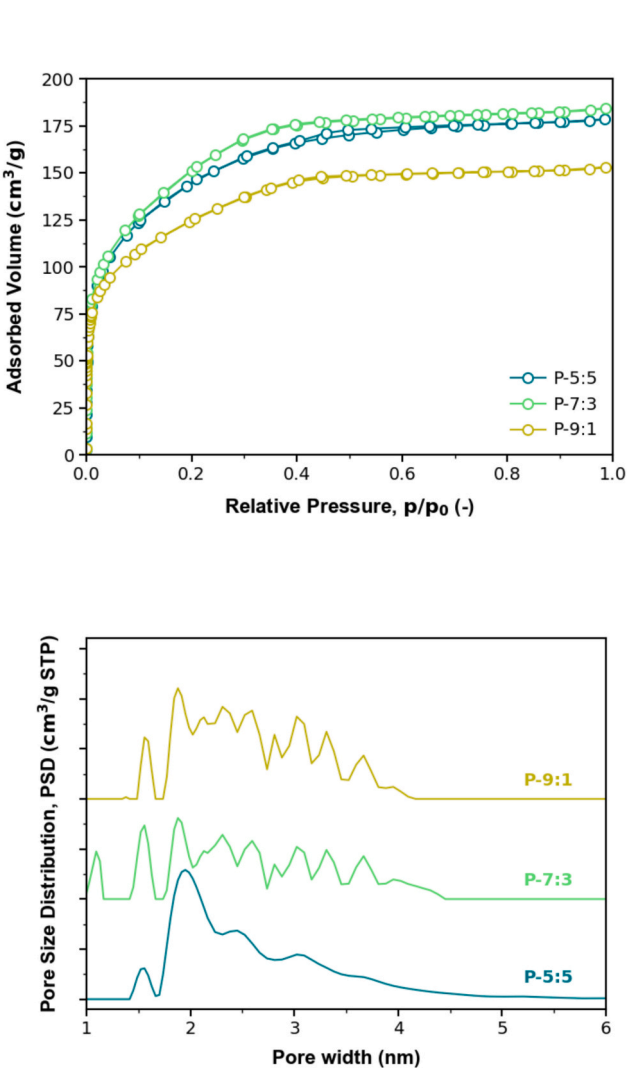

Fig. 19. a) Nitrogen sorption isotherms and b) pore size distribution of samples P-5:5, P-7:3 and P-9:1.

Table 12
Textural parameters of the samples determined from the nitrogen sorption isotherms, influenced by varying the TEOS:MTES content.

TEOS:MTES ratio	50:50	70:30	90:10
S_{BET} (m^2/g)	510	541	423
V_t (cm^3/g)	0.275	0.283	0.235
w_{max} (nm)	1.96	1.90	0.82

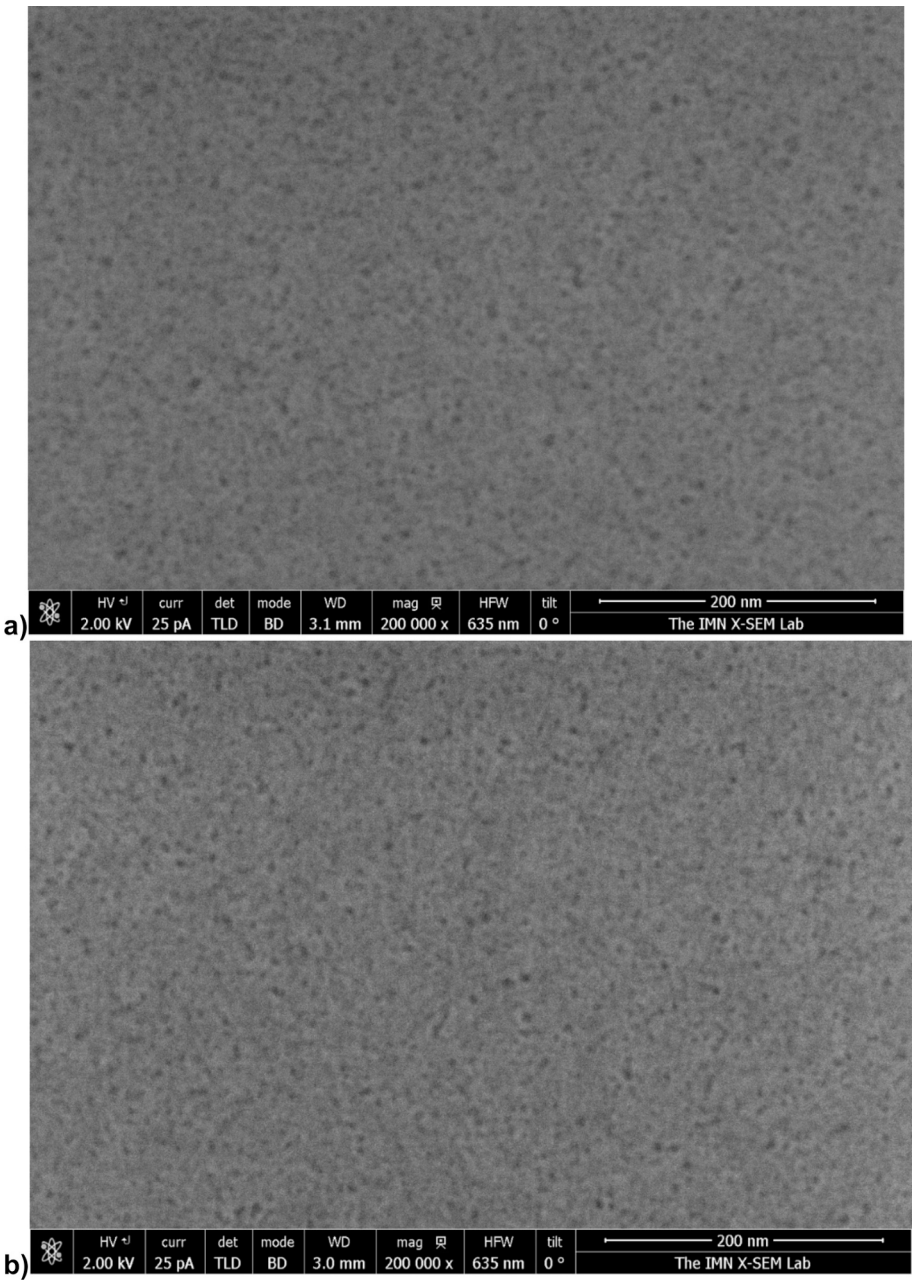

Fig. 20. Scanning electron microscope images for samples P-5:5 (a) and P-9:1 (b).

nanostructured morphology with uniformly distributed spherical domains in the 5–8 nm range. While no dramatic morphological differences are observed, the P-9:1 sample shows a slight shift towards smaller sizes, compared to predominantly larger features in P-5:5.

Overall, the correlation between nitrogen adsorption data and SEM imaging confirms the impact of precursor composition on porosity and microstructure. These findings underscore the tunability of silica coatings through precise control of precursor ratios, with implications for optimizing their optical and mechanical performance.

3.2.4. Mechanical and environmental durability

Fig. 21 shows R_a and τ_s data obtained from abrasion and accelerated aging tests. The obtained results highlight a strong dependency of the coatings' mechanical properties with TEOS:MTES ratio. Samples with lower TEOS content (P-5:5) exhibited earlier scratches formation and material detachment due to increased brittleness. In contrast, coatings with a higher TEOS fraction (P-9:1) demonstrated greater mechanical stability, maintaining surface integrity over more cycles, although it still presents gradual surface wear. In the case of P-5:5, the coating exhibits a sharp drop in R_a within the first few cycles. Surface degradation is already evident after 20 cycles, and by 50 cycles, the coating appears almost completely gone, indicating early failure and poor mechanical durability. This rapid loss of material is consistent with the higher porosity of the MTES-rich network, which provides flexibility but insufficient resistance to abrasion. P-7:3 displays intermediate behavior. The initial roughness remains relatively stable up to around 50 cycles, after which a pronounced decrease is observed. By 100 cycles, the surface shows significant smoothing, suggesting partial delamination and progressive erosion of the coating. Although more durable than P-5:5, this formulation still lacks long-term resistance under repeated mechanical stress. In contrast, P-9:1, with the highest TEOS content, exhibits the most gradual decline in R_a. Even after 150 cycles, the coating retains measurable R_a values, and signs of complete material loss only appear close to 200 cycles. This suggests a denser, more mechanically

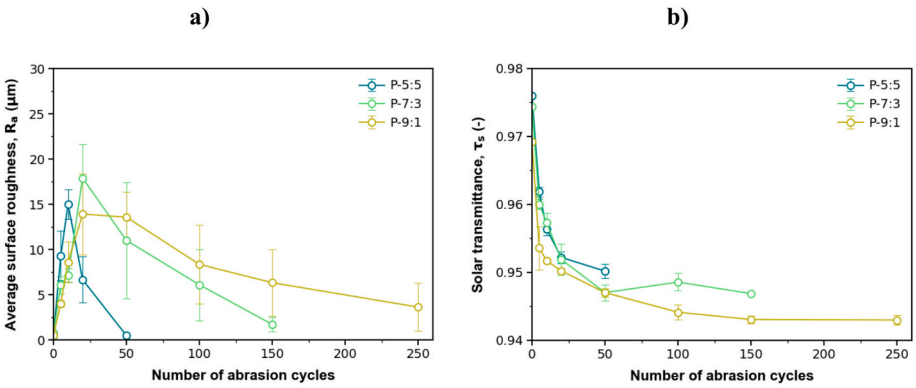

Fig. 21. Average surface roughness evolution of coatings a) and solar transmittance b) for P-5:5, P-7:3 and P-9:1 as a function of the number of abrasion cycles.

stable structure, likely due to higher crosslinking within the silica network. However, the slower degradation may also reflect a more brittle response, where material is lost progressively through micro-cracking rather than early detachment. In addition to tracking the evolution of R_a, the τ_s of the sintered samples was also measured after each abrasion interval and the measured data is shown in Fig. 21b. The observed trends closely match the roughness data, with P-5:5 showing the fastest initial decline, and P-9:1 exhibiting a more gradual decrease over the entire cycle range. Once again, none of the samples reached the transmittance level of bare borosilicate glass (~0.92) since the coatings are applied on both sides of the substrate, contributing to a slightly higher baseline even after significant material loss.

The images captured by the microscope (Fig. 22) support the information derived from the measurements of R_a and τ_s as shown in Fig. 21.

Next, the evaluation of the weathering resistance of one side coated samples is presented. The results under combined UV-condensation conditions are shown in Fig. 23 and Table 13. All coatings exhibited slight variations in τ_s and more pronounced reductions in WCA over the duration of the test. The τ_s remained relatively stable across all samples, with changes below 0.5 %. The P-9:1 sample showed a minimal variation of 0.11 %, while P-7:3 and P-5:5 presented slightly higher but still

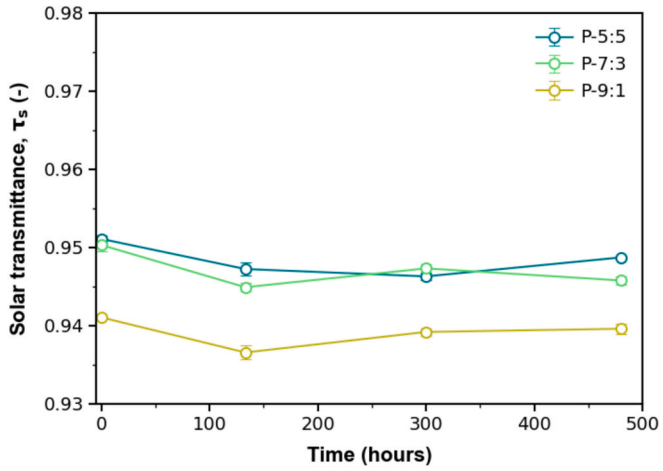

Fig. 23. Evolution of solar transmittance values for coatings subjected to combined UV radiation and condensation cycles.

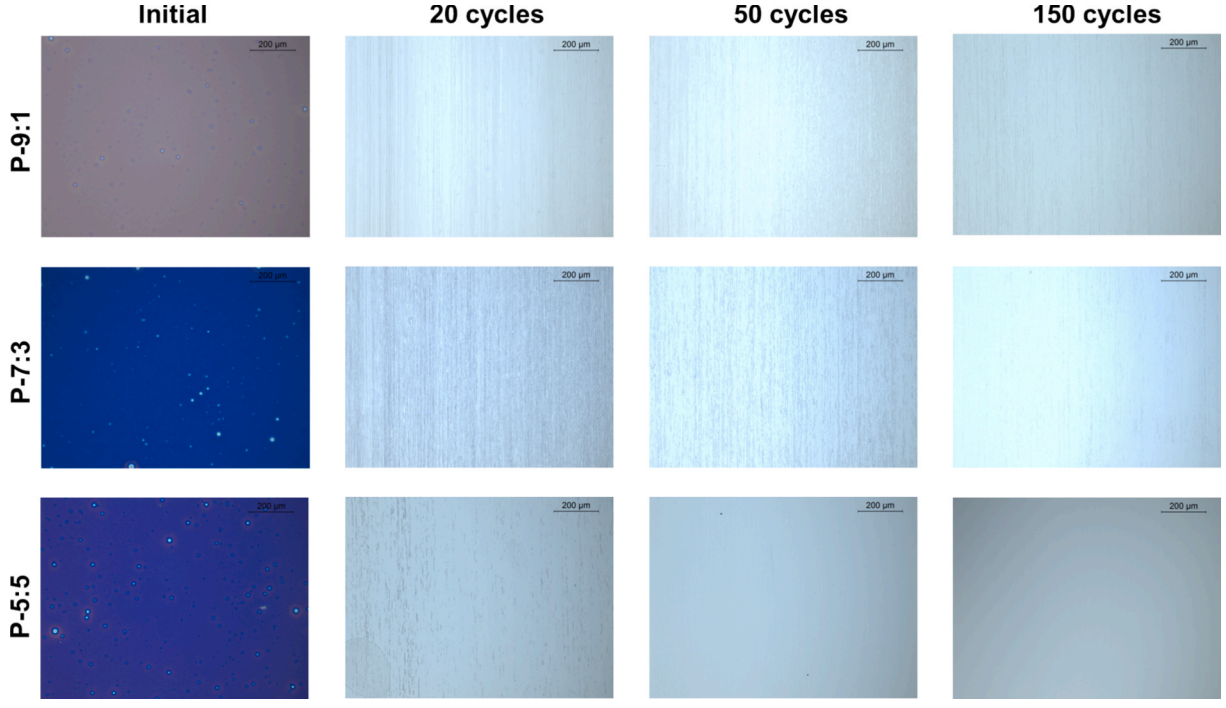

Fig. 22. Optical microscopy images of P-5:5, P-7:3, and P-9:1 before and after abrasion testing at different cycle stages (initial, 20, 50, and 150 cycles).

Table 13
Water contact angle and calculated solar transmittance measured for samples P-5:5, P-7:3 and P-9:1 during and after combination of UV radiation and condensation for 480 h.

TEOS: MTES ratio	τ_s before exp.	τ_s after 133 h exp.	τ_s after 300 h exp.	τ_s after exp. (480 h)	Change (%)	WCA before exp.	WCA after exp.	Change (%)
50:50	0.951	0.947	0.946	0.949	0.21	56	27	51.8
70:30	0.950	0.945	0.447	0.946	0.42	29	24	17.2
90:10	0.941	0.937	0.939	0.940	0.11	26	16	38.5

moderate changes of 0.42 % and 0.21 %, respectively. These values indicate that the optical functionality of the coatings is largely preserved under accelerated aging, regardless of precursor ratio.

In contrast, the WCA values experienced more substantial reductions, especially for the formulation with higher MTES content. P-5:5 displayed a drop from 56° to 27°, corresponding to a 51.8 % decrease. P-7:3 showed a smaller reduction of 17.2 %, from 29° to 24°, while P-9:1 decreased by 38.5 %, from 26° to 16°. These results suggest that although the hybrid coatings retain their optical performance over time, their surface hydrophobicity deteriorates at different rates depending on the TEOS:MTES ratio.

4. Conclusions

This study investigated the development and optimization of porous silica-based AR coatings prepared by using Pluronic® P-123 as porosity generator. The effects of pore-forming agent concentration, thermal treatment, and TEOS:MTES precursor ratio on the optical, mechanical, and environmental durability of the coatings were systematically analyzed.

The addition of Pluronic® effectively reduced the refractive index, enhancing the AR properties by increasing porosity. The lowest refractive index obtained was 1.215 for the highest Pluronic® concentration (2.5 % v/v), which corresponded to a porosity of 57 %. τ_s values as high as 0.976 were obtained with the application of this coating. High stability of the optical properties was achieved under condensation and condensation/UV exposure in all the cases. However, the increase in porosity also led to a decline in mechanical stability as reflected in the lower abrasion resistance.

Thermal treatment had a significant influence on coating performance. Samples sintered at 500 °C for 15 min maintained better abrasion resistance and structural integrity compared to those subjected to 1 h of sintering. Extended thermal exposure caused excessive burnout of the pore-forming agent, weakening the silica network and reducing its mechanical strength. The coatings sintered for 1 h showed a 30–50 % faster decline in transmittance and WCA during abrasion aging compared to their 15-minute sintered equivalents.

The TEOS:MTES ratio played a key role in determining the coatings porosity and durability. Higher TEOS content resulted in denser, more mechanically resistant coatings, but with a more reactive surface which lead to an increase in the refractive index. Conversely, increasing MTES concentration led to greater porosity and more stable surface improving optical properties but reducing mechanical robustness. Regarding environmental durability, minimal τ_s changes were observed for the three TEOS:MTES ratio studied.

Ultimately, the results emphasize that the most critical aspect in designing these coatings is achieving a balance between optical performance and long-term durability. While increasing porosity enhances AR properties, it compromises mechanical stability. Finding the optimal formulation requires careful selection of the precursor ratio, pore-forming agent concentration, and thermal treatment conditions to ensure coatings that maintain high efficiency and withstand real-world operational challenges in solar thermal applications. Our results indicate that P-2.0 is the most suitable candidate, as it exhibits high transmittance without compromising environmental resistance. For locations subject to severe abrasive conditions, P-70:30 emerges as the preferred option. This material preserves optical performance while providing a threefold increase in abrasion resistance compared to its P-50:50 counterpart, making it particularly suitable for such demanding environments.

Funding and acknowledgements

This work is part of the I + D + i Project INTECSOL, PID2021-126664OB-I00, funded by MICIU/AEI/10.13039/501100011033 and by the European Regional Development funding. Also, partial funding from MEDIDA C17.I2G: CIEMAT. Nuevas tecnologías renovables híbridas, Ministerio de Ciencia e Innovación, Componente 17 "Reforma Institucional y Fortalecimiento de las Capacidades del Sistema Nacional de Ciencia e Innovación". Medidas del plan de inversiones y reformas para la recuperación económica funded by the European Union—Next Generation EU. The authors would like to thank Nuria Germán for her contribution in laboratory and characterization tasks. The authors also acknowledge the service from the MiNa Laboratory at IMN and specially Raquel Bruna, for its contribution in SEM analysis, and funding from CM (project SpaceTec, S2013/ICE2822), MINECO (project CSIC13-4–1794) and EU (FEDER, FSE). Alenka Ristić acknowledges the financial support of the Slovenian Research and Innovation Agency through the research programme Nanoporous Materials (P1-0021).

CRediT authorship contribution statement

Naia Barandica: Writing – review & editing, Writing – original draft, Visualization, Validation, Methodology, Investigation, Formal analysis, Data curation, Conceptualization. **Gema San Vicente:** Writing – review & editing, Supervision, Project administration, Methodology, Funding acquisition, Conceptualization. **Ignacio Torres:** Writing – review & editing, Investigation, Formal analysis. **Alenka Ristić:** Investigation, Formal analysis. **Aránzazu Fernández-García:** Supervision, Project administration, Methodology, Conceptualization.

Declaration of competing interest

The authors declare the following financial interests/personal relationships which may be considered as potential competing interests: Gema San Vicente reports financial support was provided by Goverment Spain Ministry science, innovation and university. If there are other authors, they declare that they have no known competing financial interests or personal relationships that could have appeared to influence the work reported in this paper.

Appendix A. Supplementary data

Supplementary data to this article can be found online at https://doi.org/10.1016/j.matdes.2026.115952.

Data availability

Data will be made available on request.

References

[1] A. Peinado Gonzalo, A. Pliego Marugán, F.P. García Márquez, A review of the application performances of concentrated solar power systems, Appl. Energy 255 (2019) 113893, https://doi.org/10.1016/j.apenergy.2019.113893.

[2] S. Lin, X. He, H. Shi, Q. He, J. Yuan, J. Duan, J. Ren, J. Liu, Comprehensive review of photovoltaic paste: materials, processing, and performance optimization, Sol. Energy Mater. Sol. Cells 295 (2026) 114013, https://doi.org/10.1016/j.solmat.2025.114013.

[3] S. Chen, Z. Li, J. Zhao, J. Xu, S. Mao, K. Chen, Self-cleaning Si/CrN nano-absorber with broadband absorption and excellent corrosion resistance for photothermal application, Mater. Des. 258 (2025) 114580, https://doi.org/10.1016/j.matdes.2025.114580.

[4] P.M. Venugopal, K.S. Manickam, A. Munimathan, R. Dhairiyasamy, Enhancing solar energy efficiency through comparative analysis of photovoltaic and hybrid photovoltaic-thermal systems, Sol. Energy Mater. Sol. Cells 292 (2025) 113806, https://doi.org/10.1016/j.solmat.2025.113806.

[5] O. Gohar, M. Zubair Khan, I. Bibi, N. Bashir, U. Tariq, M. Bakhtiar, M. Ramzan Abdul Karim, F. Ali, M. Bilal Hanif, M. Motola, Nanomaterials for advanced energy applications: recent advancements and future trends, Mater. Des., 241 (2024) 112930. https://doi.org/10.1016/j.matdes.2024.112930.

[6] M.A.R. Barno, M. Patel, S.U. Gupta, S. Hossain, S. Vo Thi, C.S. Hee, J. Kim, Aqua-powered hybrid solar cell using amorphous conformal Ga2O3 thin-film, Mater. Des. 259 (2025) 114754, https://doi.org/10.1016/j.matdes.2025.114754.

[7] M.T. Islam, N. Huda, A.B. Abdullah, R. Saidur, A comprehensive review of state-of-the-art concentrating solar power (CSP) technologies: current status and research trends, Renew. Sustain. Energy Rev. 91 (2018) 987–1018, https://doi.org/10.1016/j.rser.2018.04.097.

[8] R. Sánchez-Moreno, G. San Vicente, F. Sutter, Á. Morales, J. Wette, M. Farchado, N. Barandica, I. Cañadas, G. Saliou, A. Fernández-García, 1 - Recent developments in optical materials for concentrated solar thermal energy, in: M. Jeguirim (Ed.), Sustainable Development of Renewable Energy, Academic Press, 2024, pp. 3–35.

[9] R. Huang, T. Zhou, Q. Lu, L. Hu, P. Liu, B. Hu, L. Wang, X. Wang, Research on the application of anti-reflective self-cleaning technology in photovoltaic panels, Sol. Energy Mater. Sol. Cells 294 (2026) 113920, https://doi.org/10.1016/j.solmat.2025.113920.

[10] Z. Fang, Q. Chen, J. Yuan, Bi-layered closed-pore structure anti-reflective coatings with ZnO quantum dots for further improving the solar cell efficiency, Sol. Energy Mater. Sol. Cells 294 (2026) 113936, https://doi.org/10.1016/j.solmat.2025.113936.

[11] A.-M. Mandong, A. Uzum, Fresnel calculations of double/multi-layer antireflection coatings on silicon substrates, Res. Eng. Struct. Mater. (2021), https://doi.org/10.17515/resm2020.241en1217.

[12] T. Pickering, K. Shanks, S. Sundaram, Modelling technique and analysis of porous anti-reflective coatings for reducing wide angle reflectance of thin-film solar cells, J. Opt. 23 (2021) 025901, https://doi.org/10.1088/2040-8986/abeaec.

[13] K. Watanabe, H. Sodabanlu, Y. Nakano, M. Sugiyama, Design of broadband anti-reflection coatings for III-V/Si tandem solar modules in vehicle-integrated photovoltaic application, Sol. Energy Mater. Sol. Cells 295 (2026) 113960, https://doi.org/10.1016/j.solmat.2025.113960.

[14] N. Hayati-Roodbari, S. Chwatal, G. Jakopic, W. Nemitz, P. Lichtenegger, F. Reil, P. Melchior, R. Trattnig, C. Sommer, Low-temperature preparation of nanostructured porous sol-gel anti-reflective coating for near-infrared wavelengths, Mater. Chem. Phys. 317 (2024) 129151, https://doi.org/10.1016/j.matchemphys.2024.129151.

[15] J. Zhang, J. Yuan, P. Tian, J. Mao, Q. Zhang, Preparation of gradient refractive index films on glass surface and its anti-reflection properties, J. Alloy. Compd. 972 (2024) 172831, https://doi.org/10.1016/j.jallcom.2023.172831.

[16] E. Zäll, M. Järn, S. Karlsson, H. Tryggeson, M. Tuominen, M. Sundin, T. Wågberg, Aerosol-based deposition of broadband antireflective silica coating with closed mesoporous structure, Sol. Energy Mater. Sol. Cells 250 (2023) 112078, https://doi.org/10.1016/j.solmat.2022.112078.

[17] J. Song, P. Kumar, I. Raouf, H.S. Kim, Advancements and challenges in anti-reflective coatings: a comprehensive review, J. Mater. Res. Technol. 39 (2025) 2926–2938, https://doi.org/10.1016/j.jmrt.2025.09.268.

[18] C. Agustín-Sáenz, M. Machado, J. Nohava, N. Yurrita, A. Sanz, M. Brizuela, O. Zubillaga, A. Tercjak, Mechanical properties and field performance of hydrophobic antireflective sol-gel coatings on the cover glass of photovoltaic modules, Sol. Energy Mater. Sol. Cells 216 (2020) 110694, https://doi.org/10.1016/j.solmat.2020.110694.

[19] D. Adak, R. Bhattacharyya, H.C. Barshilia, A state-of-the-art review on the multifunctional self-cleaning nanostructured coatings for PV panels, CSP mirrors and related solar devices, Renew. Sustain. Energy Rev. 159 (2022) 112145, https://doi.org/10.1016/j.rser.2022.112145.

[20] S. Jin, S. Wang, H. Feng, H. He, M. Huang, S. Jin, D. Yang, L. Wang, Mechanically robust and self-cleaning antireflective coatings for photovoltaic modules, Sol. Energy Mater. Sol. Cells 275 (2024) 113009, https://doi.org/10.1016/j.solmat.2024.113009.

[21] W. Zhang, R. Tong, X. Zhao, W. Gao, X. Wang, X. Yang, Influence of annealing atmosphere on optical and electrical properties of Ga and F co-doped ZnO thin films prepared by sol-gel spin-coating, Mater. Today Commun. 52 (2026) 114926, https://doi.org/10.1016/j.mtcomm.2026.114926.

[22] R. Huang, L. Tang, L. Tan, A green chemistry approach to the facile and scalable synthesis of antibacterial Fe-doped ZnO nanoparticles for industrial and commercial applications, Mater. Des. 260 (2025) 115128, https://doi.org/10.1016/j.matdes.2025.115128.

[23] W. Jin, X. Tan, Q. Dai, T. Li, L. Jiang, T. Xiao, W. Chen, Simple synthesis of weather-resistant and self-cleaning anti-reflective coating for enhancing photovoltaic conversion efficiency, Mater. Sci. Semicond. Process. 184 (2024) 108847, https://doi.org/10.1016/j.mssp.2024.108847.

[24] D.M. Campana, S. Ubal, M.D. Giavedoni, F.A. Saita, A deeper insight into the dip coating process in the presence of insoluble surfactants: a numerical analysis, Phys. Fluids 23 (2011), https://doi.org/10.1063/1.3589346.

[25] Y. Wu, Z. Shang, Z. Li, W. Zhu, L. Nie, J. Liu, Porous SiO2 antireflection film with high UV resistance, Opt. Mater. 153 (2024) 115603, https://doi.org/10.1016/j.optmat.2024.115603.

[26] G. San Vicente, R. Bayón, N. Germán, A. Morales, Long-term durability of sol–gel porous coatings for solar glass covers, Thin Solid Films 517 (2009) 3157–3160, https://doi.org/10.1016/j.tsf.2008.11.079.

[27] F. Hassan-Aghaei, M.M. Mohebi, Synthesis and characterization of novel multi-layer silica thin films with tailored mesostructure as anti-reflective coatings, Opt. Mater. 135 (2023) 113246, https://doi.org/10.1016/j.optmat.2022.113246.

[28] A.K. Padhan, V. Singh, S. Ray, R.K. Voolapalli, High-performance multi-functional solar panel coatings: recent advances, challenges, strategies and industrial aspects, RSC Appl. Polym. 3 (2024) 317–335, https://doi.org/10.1039/d4lp00295d.

[29] L.Q. Wagner, F. Breckwoldt, X. Huang, C. Kübel, X. Cheng, K. Schladitz, B. M. Smarsly, Porosity tuning in soft-templated mesoporous silica: the influence of block copolymer composition and concentration, Langmuir 41 (2025) 30948–30967, https://doi.org/10.1021/acs.langmuir.5c02750.

[30] C. Shi, H. Wang, Q. Bi, L. Li, P. Sun, T. Chen, Hierarchically porous silica prepared with anionic polyelectrolyte–nonionic surfactant mesomorphous complex as dynamic template, ACS Omega 4 (2019) 1443–1448, https://doi.org/10.1021/acsomega.8b03565.

[31] C. Agustín-Sáenz, M. Machado, A. Tercjak, Antireflective mesoporous silica coatings by optimization of water content in acid-catalyzed sol-gel method for application in glass covers of concentrated photovoltaic modules, J. Colloid Interface Sci. 534 (2019) 370–380, https://doi.org/10.1016/j.jcis.2018.09.043.

[32] A. Ábrahám, L. Kócs, E. Albert, B. Tegze, B. Szolnoki, N. Nagy, G. Sáfrán, P. Basa, Z. Hórvölgyi, Durability of microporous hybrid silica coatings: optical and wetting properties, Thin Solid Films 699 (2020) 137914, https://doi.org/10.1016/j.tsf.2020.137914.

[33] F. Wiesinger, G.S. Vicente, A. Fernández-García, F. Sutter, Á. Morales, R. Pitz-Paal, Sandstorm erosion testing of anti-reflective glass coatings for solar energy applications, Sol. Energy Mater. Sol. Cells 179 (2018) 10–16, https://doi.org/10.1016/j.solmat.2018.02.018.

[34] C. Agustín-Sáenz, J.Á. Sánchez-García, M. Machado, M. Brizuela, O. Zubillaga, A. Tercjak, Broadband antireflective coating stack based on mesoporous silica by acid-catalyzed sol-gel method for concentrated photovoltaic application, Sol. Energy Mater. Sol. Cells 186 (2018) 154–164, https://doi.org/10.1016/j.solmat.2018.06.040.

[35] K. Lange, C. Pfau, E. Grunwald, M. Schak, E. Matthes, S. Grob, M. Turek, C. Hagendorf, K. Ilse, Abrasion testing of anti-reflective coatings under various conditions, Sol. Energy Mater. Sol. Cells 240 (2022) 111732, https://doi.org/10.1016/j.solmat.2022.111732.

[36] F. Guillemot, A. Brunet-Bruneau, E. Bourgeat-Lami, T. Gacoin, E. Barthel, J. P. Boilot, Latex-templated silica films: tailoring porosity to get a stable low-refractive index, Chem. Mater. 22 (2010) 2822–2828, https://doi.org/10.1021/cm903754k.

[37] S. Yu, T.K.S. Wong, X. Hu, K. Pita, The effect of TEOS/MTES ratio on the structural and dielectric properties of porous silica films, J. Electrochem. Soc. 150 (2003) F116, https://doi.org/10.1149/1.1566021.

[38] M. Zaharescu, A. Jitianu, A. Brăileanu, J. Madarász, C.S. Novák, G. Pokol, Composition and thermal stability of SiO_2-based hybrid materials TEOS-MTEOS system, J. Therm. Anal. Calorim. 71 (2003) 421–428, https://doi.org/10.1023/A:1022883221776.

[39] G. San Vicente, R. Bayón, N. Germán, A. Morales, Surface modification of porous antireflective coatings for solar glass covers, Sol. Energy 85 (2011) 676–680, https://doi.org/10.1016/j.solener.2010.06.009.

[40] IEC TS 62862-1-1:2018, Solar thermal electric plants - Part 1-1: Terminology, (2018).

[41] B. Li, M. Gabás, E. Ochoa-Martínez, V.G. de la Cruz, M.C. López-Escalante, L. León-Reina, R. Peña, P. García-Díaz, I. García, C. Algora, Experimental optical and structural properties of ZnS, MgF_2, Ta_2O_5, Al_2O_3 and TiO_2 deposited by electron beam evaporation for optimum anti-reflective coating designs, Sol. Energy 243 (2022) 454–468, https://doi.org/10.1016/j.solener.2022.08.006.

[42] L. Hang, W. Liu, X. Zhang, S. Zhou, J. Xu, C. Li, Design and preparation of high-transmittance broadband antireflection coatings with tailored refractive indices deposited by PECVD, Vacuum 208 (2023) 111714, https://doi.org/10.1016/j.vacuum.2022.111714.

[43] M. Khardani, M. Bouaïcha, B. Bessaïs, Bruggeman effective medium approach for modelling optical properties of porous silicon: comparison with experiment, Phys. Stat. Solidi C, 4 (2007) 1986-1990. https://doi.org/10.1002/pssc.200674420.

[44] A. Ristić, N. Zabukovec Logar, New composite water sorbents $CaCl_2$-PHTS for low-temperature sorption heat storage: determination of structural properties, Nanomaterials 9 (2019) 27.

[45] S. Brunauer, P.H. Emmett, E. Teller, Adsorption of gases in multimolecular layers, J. Am. Chem. Soc. 60 (1938) 309–319, https://doi.org/10.1021/ja01269a023.

[46] A. Ristić, S.K. Henninger, Sorption composite materials for solar thermal energy storage, Energy Procedia 48 (2014) 977–981, https://doi.org/10.1016/j.egypro.2014.02.111.

[47] K.S.W. Sing, Reporting physisorption data for gas/solid systems with special reference to the determination of surface area and porosity (Recommendations 1984), 57 (1985) 603-619. http://doi.org/10.1351/pac198557040603.
[48] R. Bardestani, G.S. Patience, S. Kaliaguine, Experimental methods in chemical engineering: specific surface area and pore size distribution measurements—BET, BJH, and DFT, Can. J. Chem. Eng. 97 (2019) 2781–2791, https://doi.org/10.1002/cjce.23632.
[49] N.A. Seaton, J.P.R.B. Walton, N. Quirke, A new analysis method for the determination of the pore size distribution of porous carbons from nitrogen adsorption measurements, Carbon 27 (1989) 853–861, https://doi.org/10.1016/0008-6223(89)90035-3.
[50] Method for measuring photovoltaic (PV) glass - Part 1: Measurement of total haze and spectral distribution of haze, IEC 62805-1:2017, (2017).
[51] ISO 21920-2:2021 Geometrical product specifications (GPS) — Surface texture: Profile — Part 2: Terms, definitions and surface texture parameters, International Organization for Standardization, (2021).
[52] Standard Test Method for Film Hardness by Pencil Test, ASTMD3363-00, (2000).
[53] Z. Chen, L.Y.L. Wu, Chapter 14 - scratch damage resistance of silica-based sol–gel coatings on polymeric substrates, in: K. Friedrich, A.K. Schlarb (Eds.), Tribology of Polymeric Nanocomposites (second Edition), Butterworth-Heinemann, Oxford, 2013, pp. 467–511.
[54] X. Meng, Y. Wang, H. Wang, J. Zhong, R. Chen, Preparation of hydrophobic and abrasion-resistant silica antireflective coatings by using a cationic surfactant to regulate surface morphologies, Sol. Energy 101 (2014) 283–290, https://doi.org/10.1016/j.solener.2013.12.038.
[55] S.A. Mahadik, M.S. Kavale, S.K. Mukherjee, A.V. Rao, Transparent Superhydrophobic silica coatings on glass by sol–gel method, Appl. Surf. Sci. 257 (2010) 333–339, https://doi.org/10.1016/j.apsusc.2010.06.062.
[56] V. Purcar, V. Rădiţoiu, F.M. Raduly, A. Rădiţoiu, S. Căprărescu, A.N. Frone, C.-A. Nicolae, M. Anastasescu, Investigation of hybrid films based on fluorinated silica materials prepared by sol–gel processing, Coatings 12 (2022) 1595, https://doi.org/10.3390/coatings12101595.
[57] M. Nguyen-Quang, F. Azzolina-Jury, F. Thibault-Starzyk, A. Travert, M. Ziąbka, B. Samojeden, M. Motak, P. Da Costa, Unveiling the potential of surfactant pluronic-P123 application during the synthesis of Ni-hydrotalcite-derived catalysts for low-temperature CO_2 methanation: a novel approach, Appl. Mater. Today 32 (2023) 101805, https://doi.org/10.1016/j.apmt.2023.101805.
[58] F. Bérubé, S. Kaliaguine, Calcination and thermal degradation mechanisms of triblock copolymer template in SBA-15 materials, Microporous Mesoporous Mater. 115 (2008) 469–479, https://doi.org/10.1016/j.micromeso.2008.02.028.
[59] F. Kleitz, W. Schmidt, F. Schüth, Calcination behavior of different surfactant-templated mesostructured silica materials, Microporous Mesoporous Mater. 65 (2003) 1–29, https://doi.org/10.1016/s1387-1811(03)00506-7.
[60] A. Afshar Taromi, S. Kaliaguine, Synthesis of ordered mesoporous γ-alumina – effects of calcination conditions and polymeric template concentration, Microporous Mesoporous Mater. 248 (2017) 179–191, https://doi.org/10.1016/j.micromeso.2017.04.040.
[61] L. Karlina, C. Azmiyawati, A. Darmawan, Synthesis and characterization of hydrophobic silica prepared by different acid catalysts, IOP Conf. Ser.: Mater. Sci. Eng. 509 (2019) 012065, https://doi.org/10.1088/1757-899X/509/1/012065.
[62] B. Mirtaheri, M. Shokouhimehr, A. Beitollahi, Synthesis of mesoporous tungsten oxide by template-assisted sol–gel method and its photocatalytic degradation activity, J. Sol-Gel Sci. Technol. 82 (2017) 148–156, https://doi.org/10.1007/s10971-016-4289-4.
[63] Z. Dudás, A. Len, C. Ianăşi, G. Paladini, Structural modifications caused by the increasing MTES amount in hybrid MTES/TEOS-based silica xerogels, Mater Charact 167 (2020) 110519, https://doi.org/10.1016/j.matchar.2020.110519.
[64] M. Thommes, K. Kaneko, A.V. Neimark, J.P. Olivier, F. Rodriguez-Reinoso, J. Rouquerol, K.S.W. Sing, Physisorption of gases, with special reference to the evaluation of surface area and pore size distribution (IUPAC Technical Report), Pure Appl. Chem. 87 (2015) 1051–1069, https://doi.org/10.1515/pac-2014-1117.
[65] N.S. Donanta Dhaneswara, Effect of different pluronic P123 triblock copolymer surfactant concentrations on SBA-15 pore formation, Int. J. Technol. 7 (2016) 291–319, https://doi.org/10.14716/ijtech.v7i6.3412.
[66] S.H. Joo, R. Ryoo, M. Kruk, M. Jaroniec, Evidence for general nature of pore interconnectivity in 2-dimensional hexagonal mesoporous silicas prepared using block copolymer templates, J. Phys. Chem. B 106 (2002) 4640–4646, https://doi.org/10.1021/jp013583n.
[67] J.G. Buijnsters, R. Zhong, N. Tsyntsaru, J.-P. Celis, Surface wettability of macroporous anodized aluminum oxide, ACS Appl. Mater. Interfaces 5 (2013) 3224–3233, https://doi.org/10.1021/am4001425.
[68] M. Norek, A. Krasiński, Controlling of water wettability by structural and chemical modification of porous anodic alumina (PAA): towards super-hydrophobic surfaces, Surf. Coat. Technol. 276 (2015) 464–470, https://doi.org/10.1016/j.surfcoat.2015.06.028.
[69] J. Meng, F. Yin, S. Li, R. Zhong, Z. Sheng, B. Nie, Effect of different concentrations of surfactant on the wettability of coal by molecular dynamics simulation, Int. J. Min. Sci. Technol. 29 (2019) 577–584, https://doi.org/10.1016/j.ijmst.2019.06.010.
[70] A.J. Kessman, E.E. DeFusco, A.W. Hoover, K.A. Sierros, D.R. Cairns, Structural, mechanical, and tribological properties of fluorinated mesoporous silica films: effect of functional moiety and surfactant template concentrations, Thin Solid Films 520 (2012) 3896–3903, https://doi.org/10.1016/j.tsf.2012.01.020.
[71] J. Gallardo, A. Duran, I. Garcia, J.P. Celis, M.A. Arenas, A. Conde, Effect of sintering temperature on the corrosion and wear behavior of protective SiO_2-based sol-gel coatings, J. Sol-Gel Sci. Technol. 27 (2003) 175–183, https://doi.org/10.1023/A:1023702701850.
[72] K.H. Nielsen, T. Kittel, K. Wondraczek, L. Wondraczek, Optical breathing of nano-porous antireflective coatings through adsorption and desorption of water, Sci. Rep. 4 (2014) 6595, https://doi.org/10.1038/srep06595.
[73] S. Rubeck, V. Cartailler, V. Coutellier, G. Imbert, S. Gallois-Garreignot, S. Meille, P. Steyer, J. Chevalier, Effect of accelerated hydrothermal aging on the durability of Si-based dielectric thin films, Microelectron. Eng. 264 (2022) 111858, https://doi.org/10.1016/j.mee.2022.111858.
[74] E.A. Mwafy, G.V. Kaliyannan, A.A.A. Darwish, M.M. Motawea, R. Gunasekaran, R. Rathanasamy, Z. El-Tayeb, W.B. Elsharkawy, A.M. Mostafa, S.K. Palaniappan, Enhancing solar cell productivity with $MgAl_2O_4$–$ZnAl_2O_4$ blended anti-reflection coatings, Surf. Interfaces 53 (2024) 104997, https://doi.org/10.1016/j.surfin.2024.104997.
[75] M. Barczak, M. Oszust-Cieniuch, P. Borowski, Z. Fekner, E. Zięba, SBA-15 silicas containing sucrose, J. Therm. Anal. Calorim. 108 (2012) 1093–1099, https://doi.org/10.1007/s10973-011-1973-z.
[76] Y. Zhang, C. Zhao, P. Wang, L. Ye, J. Luo, B. Jiang, A convenient sol–gel approach to the preparation of nano-porous silica coatings with very low refractive indices, Chem. Commun. 50 (2014) 13813–13816, https://doi.org/10.1039/C4CC05397D.
[77] A.-M. Putz, K. Wang, A. Len, J. Plocek, P. Bezdicka, G.P. Kopitsa, T.V. Khamova, C. Ianăşi, L. Săcărescu, Z. Mitróová, C. Savii, M. Yan, L. Almásy, Mesoporous silica obtained with methyltriethoxysilane as co-precursor in alkaline medium, Appl. Surf. Sci. 424 (2017) 275–281, https://doi.org/10.1016/j.apsusc.2017.04.121.